Ultrafast optically induced tunneling in narrow metallic gaps from the time-dependent density-functional perspective

Boyang Ma,[1,2,3] Antton Babaze,[4,5] Michael Krüger,[1,2,3] Javier Aizpurua,[6,7,8] and Andrei G. Borisov[6,9,*]

[1]*Department of Physics, Technion—Israel Institute of Technology, Haifa 32000, Israel*
[2]*Solid State Institute, Technion—Israel Institute of Technology, Haifa 32000, Israel*
[3]*The Helen Diller Quantum Center, Technion—Israel Institute of Technology, Haifa 32000, Israel*
[4]*Materials Physics Center, CSIC-UPV/EHU, Manuel de Lardizabal 5, 20018 Donostia, Spain*
[5]*Department of Applied Physics, School of Architecture, UPV/EHU, 20018 Donostia, Spain*
[6]*Donostia International Physics Center, Manuel de Lardizabal 4, 20018 Donostia, Spain*
[7]*Department of Electricity and Electronics, FCT-ZTF, UPV/EHU, B° Sarriena s/n, 48940 Leioa, Spain*
[8]*IKERBASQUE, Basque Foundation for Science, 48009 Bilbao, Spain*
[9]*Institut des Sciences Moléculaires d'Orsay (ISMO), UMR 8214, CNRS, Université Paris-Saclay, 91405 Orsay Cedex, France*

(Received 8 October 2025; accepted 2 March 2026; published 6 April 2026)

Electron tunneling through a potential barrier is a salient quantum effect behind multiple practical applications such as, for example, in electronics and scanning tunneling microscopy. Often considered within the quasistatic picture, where the tunneling current flows through the system in response to an applied dc field, electron tunneling can be brought into the realm of ultrafast phenomena when triggered by the electric field of a short optical pulse. Ultrafast scanning tunneling microscopy thus emerges as a result of the combination of the ultimate spatial and temporal resolution, offering unprecedented perspectives for studying electron and phonon dynamics at surfaces. In this work, using the time-dependent density-functional theory, we address the electron tunneling triggered by short (single-cycle and several-cycle) optical pulses in narrow metallic gaps under conditions relevant for actual experiments. We identify photon-assisted tunneling with one-photon, two-photon, and higher-order-photon absorption, and discuss the effect of the tunneling barrier, applied bias, and strength of the optical field on the transition from photon-assisted tunneling (weak optical fields) to the optical-field emission at strong optical fields. Numerical single-electron calculations and an analytical strong-field theory model are implemented to gain deeper insights into the results of the time-dependent density-functional theory calculations. Additionally, our parameter-free calculations allow us to retrieve and explain recent experimental results on optically induced transport in narrow metallic gaps under an applied dc bias.

DOI: 10.1103/8mc1-jfmv

I. INTRODUCTION

Combining the atomic-scale resolution of the scanning tunneling microscope (STM) with the time resolution offered by short and intense optical pulses has given rise to the field of ultrafast scanning tunneling microscopy (USTM), which offers numerous opportunities to study intrinsic and photon-induced dynamics at surfaces [1–11]. This is without mentioning the burgeoning field of THz-assisted STM (THz STM) [12–17]. The development of experimental techniques calls for theoretical approaches capable to account for the main physical processes at play, to analyze and to explain the experimental data on a parameter-free basis, and to propose new experiments. Thus, the description of the USTM has to address the lightwave-driven electron currents in metallic junctions for a wide range of experimental conditions. The role of the size of the junction, of the applied bias, of the optical-field strength, and of the waveform of the optical transient is of interest.

For a wide gap between metals, the lightwave-induced electron transport involves electron emission into the vacuum. This process can thus be understood using theories of conventional and time-resolved photoemission from surfaces [18–20] (weak optical fields), or using theoretical approaches developed in the context of the interaction of short and intense laser pulses with metallic tips, plasmonic nanoparticles, or plasmonic structures with gaps of $\gtrsim$10 nm widths [8,21–32]. While such a wide junction might be produced in USTM, the most interesting regime of operation of the device associated with atomic-scale resolution is the tunneling regime with a nanometric size of the junction. In this situation, the lightwave-induced electron transport in the system results not only from the electron emission above the tunneling barrier separating the metal surfaces, but also from electron tunneling assisted by absorption of one or several photons, as illustrated in Fig. 1.

Lightwave-assisted electron tunneling is often discussed within the framework of the perturbative continuous-wave (cw) approximation, such as the Landauer-Büttiker theory [33,34] as well as the Tien-Gordon theory of photon-assisted tunneling (PAT) [35–38]. Using the scattering theory

*Contact author: andrei.borissov@universite-paris-saclay.fr

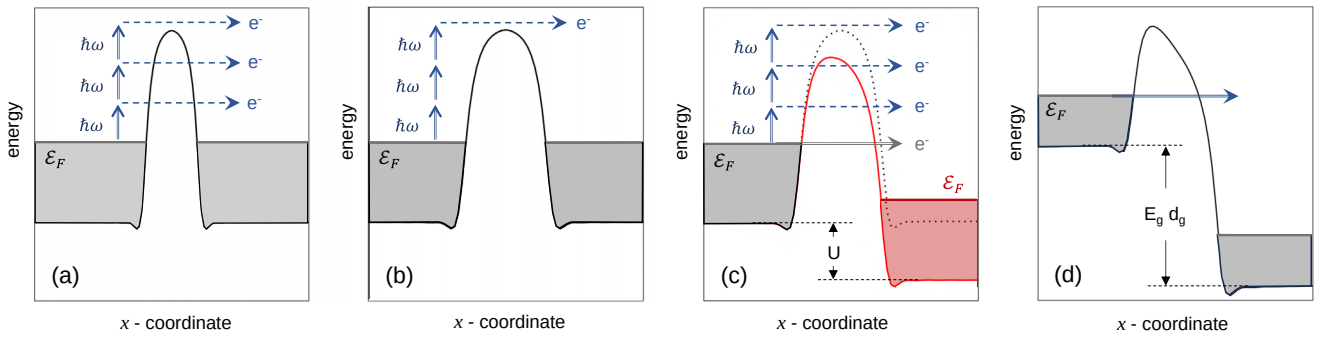

FIG. 1. Sketch of the processes behind electron transport in the gap under different conditions. The potential of the junction between two metallic leads is shown as function of the x coordinate perpendicular to the surface. $\mathcal{E}_F$ stands for the Fermi energy, $\hbar\omega$ is the energy of an absorbed photon. (a) The multiphoton regime of electron transport for narrow junction (weak fields). No bias is applied. The ℓ-photon absorption (vertical solid arrows, $\hbar\omega$) can lead to tunneling through the potential barrier reduced by $\ell\hbar\omega$ (here $\ell = 1$ or 2), or to a classically allowed over-the-barrier transition when $\ell\hbar\omega$ is larger than the height of the tunneling barrier (here $\ell = 3$). The different ℓ channels of electron transfer are shown with dashed blue arrows. (b) The same as (a), but the width of the junction is large. The electron tunneling contribution is negligible. Instead, electron transport is dominated by classically allowed over-the-barrier transitions. The process can be seen as electron emission followed by electron propagation in the vacuum gap. (c) The same as (b), but a dc bias U is applied. This reduces the potential barrier and permits tunneling. Along with over-the-barrier transitions assisted by multiphoton absorption, the dc tunneling (solid gray arrow) or tunneling induced by ℓ-photon absorption is possible. (d) The optical-field emission regime (strong fields), where an electron tunnels through the potential barrier reduced by the optical field (solid blue arrow).

formulation of Pedersen and Büttiker [34], the zero-frequency electron current $\mathcal{I}$ induced by cw light of frequency ω between two metallic leads separated by a distance $d_{\rm gap}$ results from transitions involving electronic states "dressed" by the optical field:

$$\mathcal{I} = -I_{\rm dc}(U) + \sum_{\ell=-\infty}^{\infty} J_\ell^2\left(\frac{V_{\rm g}}{\hbar\omega}\right)\int d\mathcal{E}\,T(\mathcal{E}) \times [f_L(\mathcal{E}-\ell\hbar\omega) - f_R(\mathcal{E}+U)], \quad (1)$$

where the summation runs over the electron transport channels associated with absorption ($\ell > 0$) or emission ($\ell < 0$) of ℓ photons. In Eq. (1), $\mathcal{E}$ is the electron energy, $\ell\hbar\omega$ is the electron energy change associated with the ℓ photons exchange with the field, J_ℓ is the ℓth-order Bessel function, U is the applied dc bias, $V_{\rm g} = E_{\rm g} d_{\rm gap}$ is the optical bias (with $E_{\rm g}$ the optical-field amplitude in the junction), $f_L(\mathcal{E})$ ($f_R(\mathcal{E})$) is the Fermi distribution of the left (right) lead, $T(\mathcal{E})$ is the elastic transmission coefficient, and $I_{\rm dc}(U)$ is the dc current-voltage characteristic of the tunneling junction. In the perturbative regime $E_{\rm g}$ is small, and the weight of the electron transport channels quickly decreases with increasing ℓ, indeed $J_\ell^2(\frac{E_{\rm g} d_{\rm gap}}{\hbar\omega}) \propto E_{\rm g}^{2\ell}$. Obviously, the cw approximation is not suited for short optical pulses. Furthermore, a perturbative theory does not allow one to address strong optical fields.

Equation (1) admits an interpretation where $J_\ell^2(\frac{V_{\rm g}}{\hbar\omega})$ can be seen as the probability of electron excitation by ℓ photon absorption. As a result of the ℓ photon absorption, the energies of the occupied electronic states extend up to $\mathcal{E}_F + \ell\hbar\omega$ ($\mathcal{E}_F$ stands for the Fermi energy). In this way, one arrives at another approximation often used to explain experimental data where (i) absorption of ℓ photons results in a nonequilibrium energy distribution of excited (hot) electrons, and (ii) an electron tunnels from an initial state within this nonequilibrium distribution through the static potential barrier [5,9,39–41]. Using adjustable parameters allows one to describe the experimental data [5,40,41] *a priori* without limitation in the pulse duration, as well as to incorporate transport and relaxation of excited electrons in solids and thermionic emission [42], as broadly discussed nowadays in connection with plasmon-induced chemistry [43–48]. This said, electron transport appears within this approach as an incoherent process comprising sequence of two steps. This is while a number of recent experiments report on coherent control of electron transport in narrow metal junctions and of electron emission from metal surfaces [7,31,49–55].

The coherent aspects of electron tunneling and electron emission are naturally accounted for within a theoretical framework where the excitation and emission (or tunneling) are intimately linked and cannot be separated in time. Indeed, consider the narrow gap between the metals which allows for tunneling. In this situation, the photon absorption is associated with the electron excitation into the electronic state which is delocalized in the two leads (or in metal and vacuum in the case of photoemission). The electron escape from the "parent" metal surface starts therefore as soon as the optical field couples the initial and excited electronic states [7,24,50,56–64]. The theoretical methods applied in this context are often based on the strong-field approximation (SFA) [8,65,66], which allows one to address the situation of short and intense optical pulses [23,49,56,64,67] also of interest here. Along with the SFA, methods based on semianalytical [59,60,67] or numerical [64,67–69] solution of a model one-electron Schrödinger equation for a single electron active in the transition dynamics have also been reported.

Applying the theoretical techniques described above is very enlightening as it allows one to discuss various aspects of optically induced electron transport. On the other hand, an extended parametrization of the system, *ad hoc* assumptions concerning the field screening in metal, and the often

imposed reduction of the many-body problem to the one-electron problem do not allow for robust quantitative analysis of the main mechanisms involved. This points at the interest in studying optically induced electron currents in tunneling junctions using quantum time-dependent many-body methods, particularly under conditions approaching experimental ones. The explicitly time-dependent treatment allows one to naturally describe the situation of short and intense optical driving pulses where linear approximations fail. Reducing parameters of the theory and avoiding adjustment to the experiment allows one to quantify various transport channels with the ultimate goal to predict the optimal settings (the waveform of the optical pulse, the size of the junction, and an applied bias) for a desired task of USTM.

In this work, we build on our earlier time-dependent density-functional theory (TDDFT) studies of the dynamics of the electron transport in junctions between free-electron metal surfaces. While previous implementations focused on few-nanometer and wider gaps, where electron transport is primarily governed by over-the-barrier transitions [63,70], here we explore the regime of PAT by further reducing the gap size, or lowering the barrier with an applied bias. In this regime, we can clearly identify PAT channels corresponding to one-, two-, and higher-order photon absorption processes, in full agreement with recent experiments. We address the evolution of the tunneling mechanisms with optical-field intensity of single-cycle and longer optical pulses, covering situations extending from photon-driven to field-driven transport. Importantly, once the free-electron description of the metal junction is set in the ground state by the choice of the Wigner-Seitz radius and the work function, no additional parameters are used in the theory.

To provide an analytical framework for interpretation of the TDDFT results, we extend the strong-field theory (SFT) developed in previous work [63,64,67] by incorporating a static bias. In addition, we perform model calculations based on a one-active-electron description of optically induced electron transport. By comparing parameter-free, self-consistent, many-body TDDFT results with experimental data, and by using additional insights from semianalytical and numerical model approaches, we are able to discuss the underlying physical mechanisms. We believe that this study contributes to a deeper understanding of ultrafast optically induced tunneling, the process of interest for USTM and optoelectronic applications.

The paper is organized as follows. Section I provides an introduction. Section II describes the theoretical methods used in this work. Section III presents and discusses the results for both single-cycle and longer optical pulses, with a focus on the underlying intrinsic electron dynamics. Section IV compares the theoretical findings with recent experimental data and discusses several observed phenomena in detail. Finally, Sec. V summarizes the main conclusions of the work.

Atomic units (a.u.) are used below in this paper unless otherwise stated. However, to underline that the change in electron energy results from the (multi)photon absorption, in the figures we nonetheless keep the $\hbar\omega$ notation for electron excitation energies ($\hbar = 1$ in atomic units). The electron energies are measured with respect to the vacuum level of the left lead.

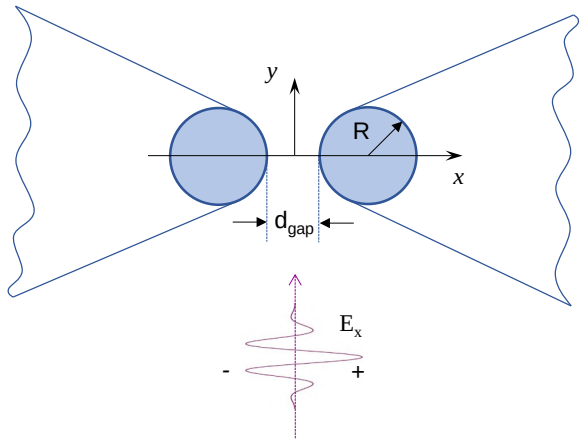

FIG. 2. Sketch of the studied system. Cross section (x, y) of a dimer of two identical parallel cylindrical nanowires (nanowire radius $R = 5$ nm) infinite along the z axis. The nanowires are separated by a narrow gap of width d_{gap} in the (sub-)nm range. The middle of the gap is located at $(x = 0, y = 0)$. An x-polarized optical pulse is incident on the nanowires along the y axis leading to optically induced electron transport across the gap. The inset shows the x component of the time-dependent electric field of the single-cycle pulse with CEP $= 0$.

II. MODEL SYSTEM AND METHODS

Below, we describe the theoretical methods used in this work to address optically induced electron tunneling and electron transport in narrow junctions between metal surfaces. Readers primarily interested in the results and their comparison with experiment, presented in Secs. III and IV, may wish to consult the beginning of Sec. II A, which introduces the system under study (see Fig. 2), and then proceed directly to Sec. II F. The latter provides a concise comparative overview of these methods and clarifies their respective contributions to this study.

A. TDDFT

While many-body approaches (including TDDFT) with a fully atomistic description of the leads have been reported in the context of lightwave-driven tunneling [7,71–73], their high computational cost explains the small size of the systems treated (far from experimental geometries) and the limited number of the phenomena considered so far. These works mainly focused on the optical-field emission regime and carrier envelope phase (CEP) dependence of the electron transport. An identification of the PAT channels associated with ℓ photon absorption and a study of their evolution with optical-field strength, gap width, and applied bias have not been performed. Being at the focus of current experimental interest [5,9,40–42,49,74,75] these aspects can be addressed using TDDFT for the electron density dynamics and a free-electron (jellium) model of the metal. The simplification of the metal description allows one to address relatively large nanoobjects relevant for actual experiments. Thus, finite-size effects as they appear, e.g., in the earlier one-dimensional (1D) study based on the configuration interaction singles method [69] can be avoided. While lacking the atomistic structure of

the metal-vacuum interface and d-band electron excitations in noble metals, the jellium TDDFT correctly captures the valence electron dynamics triggered by the optical pulses. This simple yet representative approach has been shown to predict and to semiquantitatively describe experimental findings on the optical response of plasmonic structures with narrow gaps or on electron photoemission in strong-field nanooptics [21,51,57,70,76,77].

The method employed here has been detailed in a number of publications [63,70,78]. We consider a system schematically shown in Fig. 2. Two identical parallel cylindrical nanowires of radius R are infinite along the z axis and separated by a narrow junction of width d_{gap}. We use $R = 5$ nm, which allows us to retrieve the geometry of the junction formed by bowtie antennas as studied in a number of experimental works devoted to photoemission and electron transport across nanoantenna gaps [5,58,61,70,79,80]. The electronic structure of the nanowires is modeled using the free-electron description within the stabilized jellium model [81]. The ions at the lattice sites are not treated exactly, but represented with a uniform positive background density. The density parameter is given by the Wigner-Seitz radius $r_s = 3.02$ a$_0$ typical for silver and gold (a$_0 = 1$ a.u. ≈ 0.529 Å is the Bohr radius).

The valence electron dynamics is driven by an incident x-polarized optical pulse with electric field

$$E(t) = E_0\, e^{-t^2/\tau^2} \cos(\omega t + \varphi). \tag{2}$$

Here, φ is the CEP of the pulse, and τ is the pulse duration. In Fig. 2, we show $E(t)$ for a single-cycle optical pulse with $\varphi = 0$ and $\tau = 0.85T$, where $T = \frac{2\pi}{\omega}$ is the optical period. To study the system evolution in time we employ the Kohn-Sham (KS) scheme of TDDFT and the adiabatic local density approximation (ALDA) [82] with the exchange–correlation kernel of Gunnarsson and Lundqvist [83]. Retardation effects are neglected because of the small relevant size of the system. The time-dependent electron density $n(\mathbf{r}, t)$ and the time-dependent electron current density $\mathbf{j}(\mathbf{r}, t)$ are sought as

$$\begin{aligned} n(\mathbf{r}, t) &= \sum_{k\subset\text{occ}} \chi_k |\Psi_k(\mathbf{r}, t)|^2, \\ \mathbf{j}(\mathbf{r}, t) &= \sum_{k\subset\text{occ}} \chi_k \text{Im}[\Psi_k^*(\mathbf{r}, t)\nabla\Psi_k(\mathbf{r}, t)], \end{aligned} \tag{3}$$

where $\mathbf{r} = (x, y)$, and the system is invariant with respect to translation along the z axis. The sum runs over the initially occupied KS orbitals $\Psi_k(\mathbf{r}, t)$, the statistical factor χ_k accounts for the $\pm\frac{1}{2}$ electron spin degeneracy and the degeneracy associated with motion along the z axis, Z^* stands for the complex conjugate of the complex number Z, and Im$[Z]$ stands for the imaginary part of Z.

The time evolution of the KS orbitals is given by the time-dependent KS equations

$$i\partial_t \Psi_k(\mathbf{r}, t) = \left(-\tfrac{1}{2}\nabla^2 + V(\mathbf{r}, t) + V_{\text{opt}}(x, t)\right)\Psi_k(\mathbf{r}, t). \tag{4}$$

The potential of the optical pulse is $V_{\text{opt}}(x, t) = x\, E(t)$. The self-consistent TDDFT potential $V(\mathbf{r}, t)$ is given by the sum of several contributions

$$V(\mathbf{r}, t) = V_{\text{H}}(\mathbf{r}, t) + V_{\text{XC}}(\mathbf{r}, t) + v_{\text{stab}}(\mathbf{r}). \tag{5}$$

Here, the Hartree potential V_{H} and the exchange-correlation potential V_{XC} depend on time through the time-dependent electron density. The time-independent stabilization potential $v_{\text{stab}}(\mathbf{r})$ allows to fix the desired value of the work function Φ of the nanowires.

The KS orbitals $\Psi_k(\mathbf{r}, t)$ are represented on an equidistant mesh in (x, y) coordinates with a typical mesh step of $h_x = h_y = 0.8$ a$_0$. Equation (4) is then solved using the Fourier-grid technique [84] and short-time split-operator propagation [85] (typical time step $\Delta t = 0.125$ a.u.) as detailed elsewhere [63,70,78]. The initial conditions for the time propagation $\Psi_k(\mathbf{r}, t \to -\infty)$ are given by the occupied KS orbitals of the ground-state (gs) system $\psi_{k,\text{gs}}(\mathbf{r})$, calculated from the density-functional theory (DFT) [86] as

$$\left(-\tfrac{1}{2}\nabla^2 + V_{\text{gs}}(\mathbf{r})\right)\psi_{k,\text{gs}}(\mathbf{r}) = \mathcal{E}_k\psi_{k,\text{gs}}(\mathbf{r}). \tag{6}$$

The same exchange-correlation kernel, and stabilization potentials as in TDDFT are used so that $V_{\text{gs}}(\mathbf{r}) = V(\mathbf{r}, t \to -\infty)$. The energies of the occupied orbitals satisfy $\mathcal{E}_k \leqslant \mathcal{E}_F$.

From the calculated electron current density $\mathbf{j}(\mathbf{r}, t)$ we obtain the net electron transfer $\mathcal{N}$ per optical pulse and per nm length of the nanowire dimer. It is given by the time integral of the total current through the $(x = 0, y, z)$ plane located at the middle of the junction

$$\mathcal{N} = \int dt \int dy\, \hat{e}_x \cdot \mathbf{j}(x = 0, y, t) \times \frac{\text{nm}}{\text{a}_0}, \tag{7}$$

where $\hat{e}_x$ is the unit length vector in the positive direction of the x axis. The last term accounts for the unit conversion. With this definition, $\mathcal{N}$ is positive (negative) when electrons are transferred in the positive (negative) direction of the dimer axis (x axis).

In addition to the case where the net electron transfer is only possible due to the dimer symmetry break by the optical field of a single-cycle laser pulse, we also investigate the role of an applied dc bias. The dc bias breaks the symmetry of the dimer and enables the net optically induced electron transfer even for longer optical pulses. Accordingly, in addition to the optical pulse given by Eq. (2), the dimer is subjected to a slowly varying external THz field directed along the negative x axis. In Eq. (4) this is implemented by replacing $V_{\text{opt}}(x, t)$ with $V_{\text{opt}}(x, t) + V_{\text{THz}}(x, t)$, where the potential owing to the THz field, $V_{\text{THz}}(x, t)$, is slowly switched on from zero to a constant value reached at time t_-, prior to the arrival of the optical pulse. The resulting effective dc bias U is defined as the difference between the self-consistent potentials inside the left and right cylinders at $t = t_-$. Further details are given in Appendix A.

When only the THz pulse is present and no optical field is applied, for $t > t_-$ the system reaches the steady state where the effective dc bias U leads to a small (in our conditions) tunneling electron current density $\mathbf{j}_U(\mathbf{r}, t)$. When optical and dc fields are acting on the system simultaneously, the electron current density $\mathbf{j}(\mathbf{r}, t)$ given by Eq. (3) includes the effect of both. Since in this work are interested in the optically induced electron transport, we therefore introduce the optically induced electron current density as $\mathbf{j}_{\text{opt}}(\mathbf{r}, t) = \mathbf{j}(\mathbf{r}, t) - \mathbf{j}_U(\mathbf{r}, t)$, and we use $\mathbf{j}_{\text{opt}}(\mathbf{r}, t)$ instead of $\mathbf{j}(\mathbf{r}, t)$ in Eq. (7) to obtain the optically induced net electron transfer $\mathcal{N}$. Note that this correction is only essential to disentangle the $\ell = 1$

electron tunneling channel, assisted by one-photon absorption at low optical-field strengths. In the multiphoton regime, $\mathbf{j}_U(\mathbf{r},t)$ is negligible in our conditions.

To simplify control of the time-dependent electric field in the gap via the incident pulse waveform, the present system is designed so that the dipolar plasmon of the nanowire dimer is off resonant with the incident optical pulse [63]. As a result, the time-dependent electric field along the dimer axis at the center of the narrow gap is free from the plasmon ringing effects, and it can be approximated as

$$E_{\rm gap}(t) = \mathcal{R}E(t) = E_{\rm g}\, e^{-t^2/\tau^2}\cos(\omega t+\varphi), \tag{8}$$

where $\mathcal{R}$ is the field enhancement. To set the order of magnitude, $\mathcal{R}\approx 4$ for $d_{\rm gap}=1$ nm and $\mathcal{R}\approx 3$ for $d_{\rm gap}=2$ nm, within the range of other parameters (frequency, bias, metal work function) encompassed in this work.

When relating our model system to experimentally accessible devices, such as bowtie antennas or STM junctions, it is important to note that the strongly nonlinear photoemission processes in those systems are primarily governed by the gap region, where the electric field enhancement is the strongest. In addition, PAT is highly sensitive to the height and width of the potential barrier, both of which are minimized along the shortest path between metal leads (the x-axis in our geometry). One thus can conclude that the electron transfer between nanowires owing both to the tunneling and photoemission is determined by the current flowing through the junction [63,70]. This observation has two important implications. First, as discussed in our earlier work [63], the field amplitude $E_{\rm g}=\mathcal{R}E_0$ is the relevant parameter to characterize the lightwave-induced electron transfer, which we will refer to throughout this paper. Second, the parallel nanowire configuration addressed here is representative for understanding ultrafast electron dynamics in more complex nanostructures. In particular, the TDDFT results obtained here are relevant to narrow-gap bowtie antennas [5,70,79] and to optically driven STM junctions [5,40–42,49], which constitute one of the main motivations for this work.

B. One-active-electron approach

In addition to the many-body TDDFT calculations, we also use a simplified one-dimensional model based on the single-active-electron approximation, as often employed to analyze multiphoton and optical-field emission regimes in the context of electron emission from nanotips or transfer across metallic gaps [8,30,31,49,56,58,60,64,67,69,87]. Despite its simplicity, where often (but not always [68,88,89]) the entire valence band is represented by a single orbital, and *ad hoc* screening of the optical field is imposed, the method allows one to grasp the qualitative physical effects involved in the transport process with minimal computational cost. It also provides direct access to intuitive information such as the single-particle dynamics, which is masked in fully many-body TDDFT simulations.

The method, referred to here as wave-packet propagation (WPP) approach, is based on the solution of the one-electron time-dependent Schrödinger equation (TDSE) for an electron active in the lightwave-induced transport through the junction between the two one-dimensional potential wells representing the metallic leads. A detailed description of this technique can be found elsewhere [63]. In brief, the wave function $\psi(x,t)$ of an electron "active" in optically induced transitions and initially occupying the Fermi level of one of the leads evolves in time according to

$$i\partial_t\psi(x,t) = \left(-\frac{1}{2}\frac{\partial^2}{\partial x^2} + V_{\rm m}(x) + \tilde{V}_{\rm opt}(x,t)\right)\psi(x,t), \tag{9}$$

where $V_{\rm m}(x)$ is the model potential describing the electron-metal interaction, and $\tilde{V}_{\rm opt}(x,t)$ is the model potential of the optical pulse. We use a tilde notation to distinguish between the model potential in 1D WPP calculations and that in TDDFT. Equation (9) is solved in real time using the Fourier-grid technique [84] and short-time split-operator propagation [85].

The model potential describing electron-metal interaction $V_{\rm m}(x)$ is set using the classical electrostatic theory for an electron moving in the vacuum gap between two metal surfaces [63,90]. This potential accounts for the effect of the long-range polarization interaction by incorporating classical image potentials created by the metal surfaces

$$V_{\rm m}(x) = -v_{\rm m}(x_1) - v_{\rm m}(x_2) + \theta(d_{\rm gap}-2|x|) \times \frac{1}{4}\sum_{f=1}^{\infty}\frac{1}{f d_{\rm gap}}\left[\frac{x_1}{f d_{\rm gap}+x_1} + \frac{x_2}{f d_{\rm gap}+x_2}\right], \tag{10}$$

where $x_1 = d_{\rm gap}/2 + x$ and $x_2 = d_{\rm gap}/2 - x$ are the electron distances from classical image planes at $x_{\rm im} = \mp d_{\rm gap}/2$, and $\theta(x)$ is the Heaviside step function. The free-electron model potential $v_{\rm m}(x)$ proposed in Ref. [91] to describe the photoemission from metals smoothly connects the image potential tail $-1/4(x-x_{\rm im})$ for an electron in vacuum above the metal ($x \gg x_{\rm im}$) with a constant potential inside the metal ($x \ll x_{\rm im}$). Obviously, this model is only applicable for sizes of the junction $d_{\rm gap}$ such that the overlap between the electron densities of the nanowires is small, as it is the case in this study.

The model potential of the optical pulse $\tilde{V}_{\rm opt}(x,t)$ accounts for the field screening inside the metal.

$$\tilde{V}_{\rm opt}(x,t) = \begin{cases} x\, E_{\rm gap}(t), & |x| \leqslant \frac{d_{\rm gap}}{2}, \\ \frac{d_{\rm gap}}{2}\,\mathrm{sgn}(x)\, E_{\rm gap}(t), & |x| > \frac{d_{\rm gap}}{2}. \end{cases} \tag{11}$$

The optical field inside the gap, $E_{\rm gap}(t)$, is given by $E_{\rm gap}(t) = E_{\rm g}\, e^{-t^2/\tau^2}\cos(\omega t+\varphi)$. Although similar in form to Eq. (8), there is an important difference: in Eq. (8), $E_{\rm g}$ is calculated self-consistently via TDDFT. It accounts for the incident and induced field. Here, by contrast, $E_{\rm g}$ is introduced directly into the WPP calculation as a free parameter.

If the bias U is applied across the junction, the static field of the bias $E_{\rm bias} = -U/d_{\rm gap}$ is added to $E_{\rm gap}(t)$ in Eq. (11). In this situation, similar to the strategy used in TDDFT, we calculate both the total probability current density $j(x,t)$ and the component induced solely by the optical field $j_{\rm opt}(x,t)$. From $j_{\rm opt}(x,t)$, we obtain the electron transfer probability per optical pulse $\mathcal{P} = \int j_{\rm opt}(x=0,t)dt$, which characterizes the lightwave-driven transport in the system.

TABLE I. Differences between the metal work function Φ_M and work function Φ to be used in the ALDA TDDFT in order to account for the effect of the image charge potential in the gap.

d_{gap}, nm	0.8	1	1.6	2	4	6	∞
$\Phi_M - \Phi$, eV	0.84	0.82	0.61	0.50	0.25	0.17	0

C. Consistency between TDDFT and WPP via choice of the metal work function

As we discussed in Sec. II A, the present implementation of TDDFT employs a local exchange–correlation potential. This choice is dictated by numerical efficiency and it makes it possible to address metallic nanowires of large radii. The price to pay is that the ALDA fails to reproduce the long-range polarization potential (image potential) felt by an electron moving in vacuum in front of a metal surface [92,93]. The electron-surface interaction is too short ranged, resulting in an overestimation of the height of the tunneling barrier separating metal surfaces.

In our earlier work [63], we demonstrated that this issue can be alleviated to a large extent by a proper choice of the stabilization potential [81], and thus of the work function Φ of the nanowires obtained from ground-state DFT calculations. In practice, one requires that the height of the tunneling barrier $\mathcal{W}_{tb}$ within DFT is the same as that between actual metals obtained classically with account of the image potential (with no bias is applied):

$$\begin{aligned}\mathcal{W}_{tb} &= \Phi_M + V_m(x=0)\\ &= \Phi + V_{gs}(x=0, y=0).\end{aligned} \tag{12}$$

Here, Φ_M is the actual work function of the considered metal (in this work, silver or gold), V_{gs} is the ground-state potential calculated using DFT, and V_m is the model potential given by Eq. (10). In deriving Eq. (12), we consider that the maximum of the tunneling barrier along the shortest path between metals is attained at the middle $(x = 0, y = 0)$ of the symmetric junction. From Eq. (12) it follows that

$$\Phi = \Phi_M - [V_{gs}(x=0, y=0) - V_m(x=0)]. \tag{13}$$

The relation between Φ and Φ_M is given in Table I for the d_{gap} values relevant for this work. It is worth noting that the work function correction does not affect the qualitative aspects of the studied processes. It is important when comparing TDDFT and WPP results (in WPP, the actual work function value Φ_M is used), as well as when comparing theoretical results with experimental data obtained for a specific metal.

We verified that once conditions for Φ given by Eqs. (12) and (13) are satisfied, the heights of the DFT and model tunneling barriers are also approximately equal when the dc bias is applied. In this situation, $\mathcal{W}_{tb}$ obtained from the TDDFT is defined as

$$\mathcal{W}_{tb} = -\Phi - V_{max}^{TDDFT}, \tag{14}$$

where V_{max}^{TDDFT} is the maximum self-consistent potential in the junction obtained at $t = t_-$, i.e., at constant THz field prior to the arrival of the optical pulse [see Eqs. (A1) and (A2)]. As a final remark, the self-consistent potential $V_{gs}(x, y = 0)$ and the model potential $V_m(x)$ within the gap are quite similar along the dimer axis up to the energy offset given by $V_{gs}(x = 0, y = 0) - V_m(x = 0)$ [63] [see Eq. (13)].

D. Semiclassical strong-field theory (SFT)

Beyond the many-body self-consistent TDDFT and the one-electron WPP approach introduced above, we also employ a strong-field theoretical model developed in earlier works [64,67]. One of the prominent advantages of SFT is its ability to provide a semiclassical description which offers analytical insights into the photoemission and electron transport processes. Like the WPP approach (Sec. II B), the SFT model is based on the single-active-electron approximation and focuses on the evolution of the wave function within the junction between two metallic leads. By solving the TDSE in Eq. (9), the tunneling amplitude $M_{\mathcal{E}}$ for the electron transition from an initial state in the left lead to the final state at energy $\mathcal{E}$ in the right lead is expressed as

$$\begin{aligned}M_{\mathcal{E}} = \frac{i}{2}\int_{-\infty}^{\infty}\Big[&\Psi_{gap}(x,t)\frac{\partial}{\partial x}\psi^*(x,t)\\ &- \psi^*(x,t)\frac{\partial}{\partial x}\Psi_{gap}(x,t)\Big]\Big|_{x=-d_{gap}/2}^{x=d_{gap}/2} dt,\end{aligned} \tag{15}$$

where $\psi^*(x,t)$ and $\Psi_{gap}(x,t)$ are wave functions that evolve inside the contact metal (right) and the junction, respectively. The notation $[\dots]|_{x=-d_{gap}/2}^{x=d_{gap}/2}$ at the end of Eq. (15) stands for the subtraction of the expression inside the brackets evaluated at $x = -d_{gap}/2$ from the expression evaluated at $x = d_{gap}/2$. This formulation captures the instantaneous projection of the junction wave function onto the metallic lead region throughout the time evolution. The transport from the right to the left metal lead is evaluated using the same formula, but the signs of both the optical field and the spatial coordinate must be reversed.

Here, we only focus on the transfer of the electron initially localized at the Fermi level of the left lead to the right lead. Equation (15) provides only a formal solution to the TDSE. To analytically derive the dynamical behavior of the system, the wave functions $\psi^*(x,t)$ and $\Psi_{gap}(x,t)$ are approximated using the eigenfunctions of the metal and the Van Vleck propagator, respectively [64]. By applying the saddle-point method [56,64], the electron transfer probability $\mathcal{P}_{L\to R}$ is obtained as

$$\mathcal{P}_{L\to R} = \sum_{\mathcal{E}} |M_{\mathcal{E}}|^2 \propto \sum_{\mathcal{E}} e^{-2\mathrm{Im}[S(t_{2s},t_{1s})]}, \tag{16}$$

where $\mathrm{Im}[S(t_{2s}, t_{1s})]$ is the imaginary part of an action function $S(t_{2s}, t_{1s})$ taken at the stationary points t_{1s} (t_{2s}) of the emission (transmission) time. The action function is given by

$$\begin{aligned}S(t_{2s}, t_{1s}) = \mathcal{E}t_{2s} + \frac{\tilde{p}^2}{2}(t_{2s} - t_{1s}) - \int_{t_{1s}}^{t_{2s}} \frac{A_{opt}^2(t')}{2}\, dt'\\ - \int_{t_{1s}}^{t_{2s}} V_m[x(t')]\, dt' - \mathcal{E}_F t_{1s},\end{aligned} \tag{17}$$

where $\mathcal{E}$ is the final energy of the transported electron at the transmission time t_{2s}, $\mathcal{E}_F$ is the initial energy (Fermi energy) at the emission time t_{1s}, $A_{opt}(t) = -\int^t [E_{gap}(t') + E_{bias}]dt'$ is the vector potential of the combined enhanced optical field

and static bias, and $\tilde{p} = \frac{-\int_{t_{1s}}^{t_{2s}} A_{opt}(t')\,dt' + d_{gap}}{t_{2s}-t_{1s}}$ is the canonical momentum of the transported electron driven by the field. As a consequence of the saddle-point technique, the times t_{1s} and t_{2s} are not real-valued physical times but complex values obtained by solving the following three saddle-point equations:

$$\frac{\left[\tilde{p} + A_{opt}(t_{1s})\right]^2}{2} + \overline{V}_m = \mathcal{E}_F, \tag{18}$$

$$\int_{t_{1s}}^{t_{2s}} [\tilde{p} + A_{opt}(t')]\,dt' = d_{gap}, \tag{19}$$

$$\frac{\left[\tilde{p} + A_{opt}(t_{2s})\right]^2}{2} + \overline{V}_m = \mathcal{E}, \tag{20}$$

where $\overline{V}_m = (d_{gap})^{-1} \int_{-d_{gap}/2}^{d_{gap}/2} V_m(x)\,dx$ is the average image potential.

The three saddle-point equations above provide a three-step description of electron transport in the nanojunction:

(1) *Emission*: The bound electron is freed from the parent lead by the external field. Equation (18) describes the energy conservation at this instant. The image potential lowers the junction barrier.

(2) *Propagation*: The freed electron is accelerated by the driving field, while moving across the nanojunction [Eq. (19)]. The force from the image potential is neglected due to its weak effect in this step.

(3) *Transmission*: The energy gained in the second step is carried by the electron transferred to the opposite metallic lead [Eq. (20)].

It should be stressed that the initial energy is negative, leading to complex values of t_{1s}, $\tilde{p}$, and t_{2s}. The imaginary part of the emission time t_{1s} corresponds to purely quantum processes, such as photon absorption and tunneling through the barrier, which are not allowed in the classical dynamics. In contrast, the imaginary component of the arrival time t_{2s} is usually related to amplitude attenuation of the transported wave-function component [64,67].

E. Effect of an applied bias within SFT

Here we extend the SFT to the scenario where a dc bias field with strength $E_{bias} = |U|/d_{gap}$ is present. As demonstrated in Ref. [64], the saddle-point equations (18)–(20) allow for two types of solutions characterized by different imaginary-time durations. These are given by

$$\mathrm{Im}[t_L] = \frac{E_g\sqrt{1+\gamma^2}}{E_{bias} + E_g\sqrt{1+\gamma^2}} \frac{\ln(\gamma + \sqrt{1+\gamma^2})}{\omega} \tag{21}$$

and

$$\mathrm{Im}[\tau_L] = \mathrm{Im}\left[\frac{2d_{gap}}{\sqrt{2(\mathcal{E} - \overline{V}_m)} + i\sqrt{2\overline{\mathcal{W}}_{tb}}}\right], \tag{22}$$

where $\mathcal{E}$ is the final electron energy in the right metallic lead, $\mathcal{E} - \overline{V}_m$ is the effective final energy, and

$$\overline{\mathcal{W}}_{tb} = \overline{V}_m - \mathcal{E}_F \tag{23}$$

is the effective height of the tunneling barrier defined within SFT from the average image potential in the junction. Using $\mathcal{E}_F = -\Phi_M$, in the conditions of our study $\overline{\mathcal{W}}_{tb} \approx \mathcal{W}_{tb}$, where $\mathcal{W}_{tb}$ is defined with Eq. (12). The Keldysh parameter [94] is $\gamma = \sqrt{\overline{\mathcal{W}}_{tb}/2U_p}$ with the ponderomotive energy $U_p = [E_g/2\omega]^2$. Notice that because of the tunneling, this definition of the Keldysh parameter is different from the conventional one $\gamma = \sqrt{\mathcal{E}_B/2U_p}$ used to distinguish between photon-assisted ($\gamma \gg 1$) or optical-field-assisted ($\gamma \ll 1$) regimes of photoemission [8,30,66,95]. In the conventional definition, $\mathcal{E}_B$ is the electron binding energy, which is given, e.g., by the ionization potential in atomic physics or by the work function $\Phi_M = -\mathcal{E}_F$ in the case of photoemission from a metal. For a large gap size, the contribution of the electron-metal interaction to the tunneling barrier can be neglected, and the two definitions of γ therefore become equivalent. In the situations relevant for this study, values of γ obtained using Φ_M, Φ (see Sec. II C), or using $\overline{\mathcal{W}}_{tb}$ differ by less than 15%, so that any of them is appropriate for the qualitative purpose of distinction between electron transport regimes.

The two imaginary-time durations given by Eqs. (21) and (22) correspond to distinct types of photoemission processes. The time $\mathrm{Im}[t_L]$ of Eq. (21) describes the transition of an electron from a bound state to a laser-driven state (Volkov state). In contrast, $\mathrm{Im}[\tau_L]$ of Eq. (22) corresponds to the excitation of a bound electron to an excited eigenstate located under the potential barrier [64]. To distinguish these two regimes, we compare the time $\mathrm{Im}[t_L]$ with the extremal value of $\mathrm{Im}[\tau_L]$ ($\mathrm{Im}[\tau_e] = 2d_{gap}/\sqrt{2\overline{\mathcal{W}}_{tb}}$), and define a parameter ζ as

$$\zeta = \frac{\mathrm{Im}[t_L]}{\mathrm{Im}[\tau_e]}. \tag{24}$$

Parameters γ and ζ allow one to characterize the different regimes of electron transport in a metallic gap, as we sketch in Fig. 3 and describe below (for detailed derivations see Appendix B).

(1) For a weak optical field where $\zeta \geqslant 1$ [Fig. 3(a)], the imaginary time $\mathrm{Im}[\tau_L]$ of Eq. (22) becomes dominant. By substituting this solution into the saddle-point equations we obtain the action function $S(t_{2s}, t_{1s})$. Using $S(t_{2s}, t_{1s})$ in Eq. (16), we obtain the following key results (cf. Ref. [64]). For low bias $U \leqslant \overline{\mathcal{W}}_{tb}$,

$$\mathcal{P}_{L\to R} \propto \exp\left[-2\sqrt{2\overline{\mathcal{W}}_{tb} - (n\omega + U)}\, d_{gap}\right], \tag{25}$$

which describes the Wentzel-Kramers-Brillouin (WKB) type tunneling of an excited electron through the potential barrier of a junction in the presence of an applied bias U. In this perturbative regime PAT is dominated by the low ℓ channels [see Eq. (1)]. Consistently, the effective photon order $n = E_g d_{gap}/\omega$ is small. It tends to zero for $E_g \to 0$ where only an applied bias drives the tunneling. Indeed, $\mathcal{P}_{L\to R}$ expressed with Eq. (25) includes both electron transport owing to the applied dc bias and optically induced transitions.

For high bias $U > \overline{\mathcal{W}}_{tb}$, the electron transfer probability is given by

$$\mathcal{P}_{L\to R} \propto \exp\left[-\frac{2(2\overline{\mathcal{W}}_{tb} - n\omega)^{\frac{3}{2}}}{3E_{bias}}\right]. \tag{26}$$

Equation (26) describes the tunneling of an excited electron through a strongly suppressed triangular potential barrier,

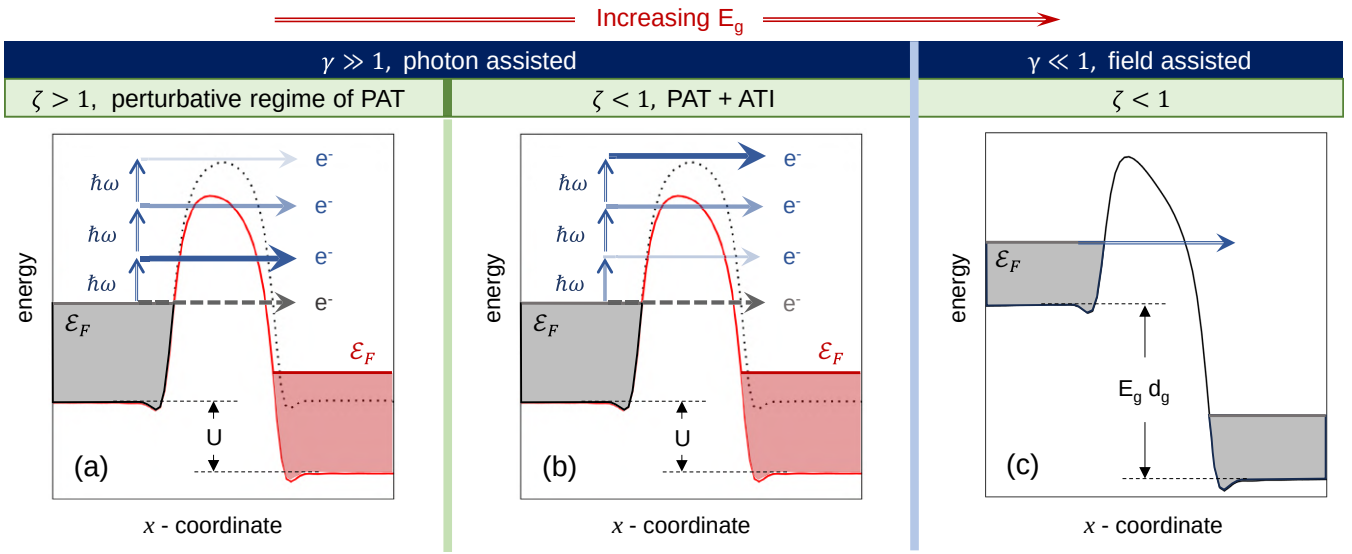

FIG. 3. Sketch of the electron transport described by the SFT. (a) When the parameter $\zeta > 1$, the electron is excited by absorbing a few photons and then tunnels through the junction. In this perturbative regime of PAT, the contribution of the ℓth channel to the transport decreases with ℓ as $E_g^{2\ell}$ [see Eq. (1)]. The photon-assisted channels do not exceed the barrier threshold so that we observe solely the PAT. (b) When $\zeta < 1$ but $\gamma \gg 1$, electron transport occurs in the multiphoton regime. The electron can absorb sufficient energy to be excited over the barrier and into a Volkov state (above-threshold ionization, ATI). The effective photon absorption reaches the barrier threshold. Although under-the-barrier PAT still occurs, it is not the dominant transport mechanism. (c) When $\zeta < 1$ and $\gamma \ll 1$, the potential barrier is adiabatically suppressed by the field, allowing the electron to efficiently tunnel through the junction.

analogous to photon-assisted Fowler-Nordheim tunneling. The effective photon order $n = E_g d_{gap}/\omega$ is given by the same expression as for the low bias case.

Equations (25) and (26) are obtained for an optical field acting as small perturbation. When E_g increases such that $\zeta < 1$, the imaginary time $\mathrm{Im}[t_L]$ becomes dominant so that the transition of an electron from a bound state to a laser-driven state (Volkov state) determines the optically induced transport across the gap [Figs. 3(b) and 3(c)]. In this situation, the Keldysh parameter γ allows for distinguishing between the multiphoton absorption and optical-field emission regimes.

(2) $\zeta < 1$, $\gamma \gg 1$. In this regime, the electron can be directly excited from the bound state to a Volkov state via multiphoton absorption [see Fig. 3(b)]. The electron transfer probability is given by

$$\mathcal{P}_{L\to R} \propto (2\gamma)^{-2n}, \tag{27}$$

where an effective number of absorbed photons

$$n = \left[\frac{\omega\sqrt{2\overline{\mathcal{W}}_{tb}}}{E_{bias} + \omega\sqrt{2\overline{\mathcal{W}}_{tb}}}\right]\frac{\overline{\mathcal{W}}_{tb}}{\omega}. \tag{28}$$

For transitions over the tunneling barrier one expects $n = \overline{\mathcal{W}}_{tb}/\omega$. However, the presence of a bias modifies the effective tunneling barrier by a factor given in square brackets. For higher-order corrections in E_{bias}, see Eq. (B9) of Appendix B.

(3) $\zeta < 1$, $\gamma \ll 1$. In this regime, both the optical field and the static bias adiabatically suppress the junction barrier, enabling tunneling [Fig. 3(c)]. The electron transfer probability follows a Fowler-Nordheim tunneling expression:

$$\mathcal{P}_{L\to R} \propto \exp\left[-\frac{2(2\overline{\mathcal{W}}_{tb})^{\frac{3}{2}}}{3(E_{bias} + E_g)}\right]. \tag{29}$$

The key difference between Eqs. (29) and (26) lies in the role of the fields. The former describes electron transfer driven by an adiabatically strong optical field and a weak static bias, while the latter describes the regime where the static bias is strong and the optical field acts as a perturbation.

We have shown previously [64] that in the regime where the optical field is strong enough so that $\zeta < 1$, the photoemission exhibits a cutoff energy determined by the work function and the parameter ζ:

$$\mathcal{E}_{cutoff} = \frac{\overline{\mathcal{W}}_{tb}}{\zeta} + \mathcal{E}_F. \tag{30}$$

The cutoff energy expression given by Eq. (30) allows for a physically transparent interpretation of the parameter ζ as $\zeta = \overline{\mathcal{W}}_{tb}/(\mathcal{E}_{cutoff} - \mathcal{E}_F)$, and provides a valuable criterion for analyzing photon absorption channels, as explored in the following sections. Indeed, the energy difference $\mathcal{E}_{cutoff} - \mathcal{E}_F$ represents the maximum energy transfer from the optical field, while the effective barrier height $\overline{\mathcal{W}}_{tb}$ represents the static binding potential. Thus, $\zeta < 1$ admits over-the-barrier, classically allowed transitions with final electron energies above the junction barrier. This is while $\zeta > 1$ corresponds to the regime where electrons with energies below the barrier $\mathcal{E}_{cutoff} - \mathcal{E}_F < \overline{\mathcal{W}}_{tb}$ tunnel across the junction.

F. Short summary of the theoretical approaches

Given the variety of theoretical tools employed, we find it useful to provide in Table II their brief summary. The main difference between the methods consists in how the electron dynamics is treated: either as that of a many-body system accounting for the entire valence band, or as that of a single electron initially at the Fermi energy. Consequently, the

TABLE II. Summary of the theoretical approaches used in this work.

Theoretical approach	Formalism and method	Electron-metal interaction	Image potential	Optical field and applied bias	Information provided
Many-body TDDFT	Numerical solution of the time-dependent Kohn-Sham equations	Self-consistent. 2D free-electron metal (FEM) Junction of the nanowire dimer	No	Self-consistent. accounts for the screening field enhancement (plasmon)	Quantitative: (1) electron density dynamics (currents, transport); (2) role of various parameters (pulse waveform, geometry, bias) in electron transport; (3) comparison with experiment
One-active-electron WPP	Numerical solution of the time-dependent Schrödinger equation	Model 1D FEM Junction between flat metal surfaces.	Model	Model. Field is set to zero inside metal	Qualitative. Used along with TDDFT: (1) analysis of the symmetry constraints to observe the one-photon channel of PAT; (2) electron final-state spectroscopy revealing ℓ-photon channels of PAT.
One-active-electron SFT	Analytical approach based on the semiclassical propagator	Model 1D FEM Junction between flat metal surfaces.	Model	Model. Field is set to zero inside metal	Analytical. Analysis of three transport regimes in TDDFT results: (1) multiphoton perturbative PAT; (2) multiphoton PAT+ATI; (3) optical-field emission.

potentials describing electron-metal and electron-field interactions are either obtained self-consistently or introduced as model potentials. In the former case, the many-body aspects such as field screening and plasmon excitations are naturally included. (Note that under conditions considered in our work, the plasmon is off resonant with the optical pulse and remains unexcited, hence the parenthesis in Table II.) In model potentials these effects are introduced *ad hoc*, using additional arguments or calculations. Model potentials, however, allow one to account for long-range polarization interactions (the image potential) acting on an electron in front of a metal surface and reducing the tunneling barrier of the junction. The present TDDFT implementation requires a correction to the metal work function to include this effect (Table I).

The main reason for using different approaches is as follows. TDDFT enables self-consistent, quantitative calculations of optically induced electron transport in metallic gaps, allowing direct comparison with experiment without adjustable parameters. Simple models, on the other hand, permit controlled variation of system parameters and facilitate the analysis of one-electron dynamics, thereby providing valuable information about the studied processes. Analytical theories are particularly useful for establishing general trends and the conditions under which those trends can be observed. Thus, while the main results presented below are obtained with quantitative many-body TDDFT, the simplified numerical (WPP) and analytical (SFT) methods provide complementary insights and are essential for a general understanding of the underlying physics.

III. ELECTRON TRANSPORT INDUCED BY AN OPTICAL PULSE

In this section, we consider electron transport induced by an optical pulse across the (sub)nanometric junction. The electric field profile of the pulse is given by Eq. (2). Unless otherwise stated, the pulse frequency is $\omega = 0.95$ eV, and $\tau = 0.85 \times 2\pi/\omega$ corresponds to a single-cycle optical pulse with a duration of 5.2 fs (intensity full width at half-maximum). The choice of the frequency and envelope of the optical pulse allows for connecting current results with earlier theoretical and experimental studies of electron transport in symmetric 1-nm and 2-nm gaps [63] as well as wider 6-nm gaps [70]. The work function of the metal Φ_M is set within the range 5–5.5 eV as reported for gold and used to describe multiphoton and optical-field emission from gold surfaces [5,76,96–98].

A. Symmetric system

We start our discussion with results obtained in the absence of an applied bias. Because of the symmetric geometry of the metallic gap, the net electron transfer results solely from the symmetry break induced by the optical field. We then obtain the well-documented sinusoidal dependence of the net electron transport on the CEP, as observed for broad vacuum gaps [8,32,99], in STM junctions [49,100], and in our recent calculations for 1-nm and 2-nm gaps [63] (see also [67]). We therefore do not show these results here. We focus our study on identifying and discussing signatures of PAT. To this end, we present results calculated for CEP $= \pi$ and CEP $= 0$, which lie approximately at the extrema of net electron transport in the positive and negative x directions, respectively. Notably, in addition to the discussion of PAT, these data allow for an estimate of the oscillation amplitude in the CEP dependence of the net electron transport.

In Fig. 4(a) we analyze the net electron transfer $\mathcal{N}$ calculated with TDDFT for gap sizes $d_{\text{gap}} = 0.8$, 1, and 2 nm. The CEP $= \pi$ of the single-cycle optical pulse is such that the maximum $\mathcal{N}$ is reached in the positive direction of the dimer x axis [63]. In the inset of Fig. 4(a) we show the time evolution of the corresponding electric field of the pulse. Obviously, the sign of $\mathcal{N}$ is reversed for CEP $= 0$. The TDDFT results for $\Phi_M = 5$ eV are shown as a function of the amplitude of the field in the gap E_g (lower x-axis) and of the Keldysh parameter defined as $\gamma = \sqrt{\Phi/2U_p}$.

For the 2-nm-wide junctions the potential barrier is too broad to allow for notable electron tunneling. Within the studied range of the optical fields the electron transfer between

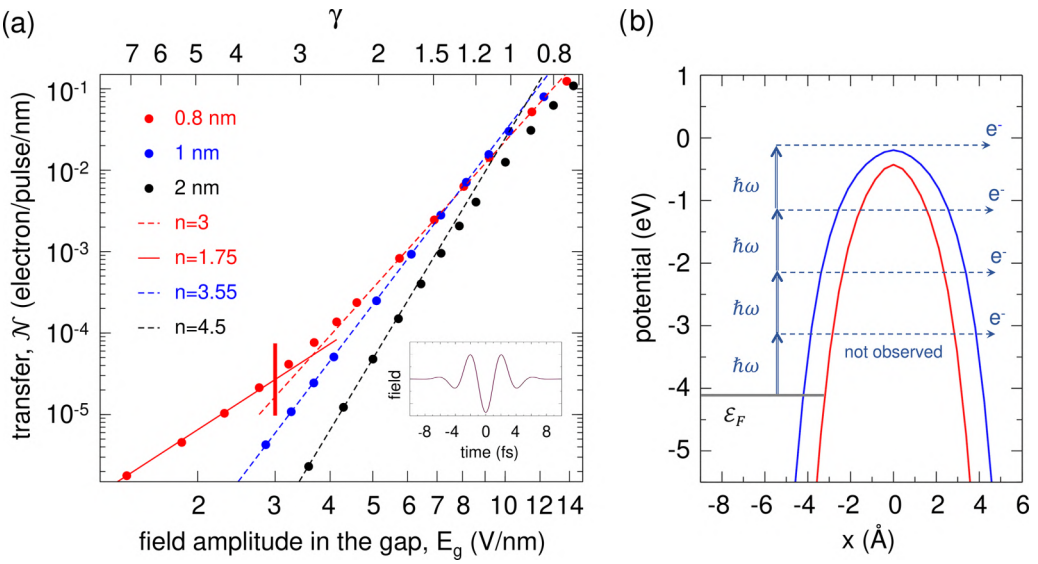

FIG. 4. Electron transfer induced by a x-polarized single-cycle optical pulse ($\omega = 0.95$ eV, CEP $= \pi$) across the gap of a nanowire dimer with work function $\Phi_M = 5$ eV. The electric field of the pulse is shown in the inset of (a). (a) Electron transfer $\mathcal{N}$ defined as the net number of electrons transferred per pulse and per nm length of the dimer. TDDFT results (dots) calculated for a width of the gap of 0.8 nm (red), 1 nm (blue), and 2 nm (black) are shown as a function of the electric field in the gap E_g and of the Keldysh parameter γ. The lines of the corresponding color display the fit by the $\mathcal{N} \propto E_g^{2n}$ dependence characteristic for the multiphoton regime. The effective number of photons n is given in the legend. The vertical red bar marks the regime transition at $\zeta = 1$ for the 0.8-nm gap. (b) Self-consistent ground-state potential $V_{gs}(x, y = 0)$ in the gap region as a function of the x coordinate along the dimer axis. Results are shown for a gap of the width of 0.8 nm (red) and 1 nm (blue). The energy is measured with respect to the vacuum level. $\mathcal{E}_F = -\Phi$ is the Fermi level energy corresponding to the effective work function $\Phi = 4.2$ eV used in the TDDFT (see Table I). Dashed arrows indicate electron tunneling and over-the-barrier transitions induced by ℓ-photon absorption. The latter is indicated with vertical arrows. The $\ell = 1$ tunneling channel is not observed in TDDFT results in (a).

the nanowires is then dominated by classically allowed over-the-barrier transitions where the n-photon absorption leads to photoexcited electron energies above the potential barrier of the junction, similar to that discussed earlier [63,70]. Indeed, fitting the optically induced net electron transfer $\mathcal{N}$ with $\mathcal{N} \propto E_g^{2n}$ dependence, we obtain in Fig. 4(a) that in the multiphoton regime the effective number of photons absorbed by transferred electron (the photon order) is $n = 4.5$. This roughly corresponds to Φ/ω. At large field strength ($\gamma \lesssim 1$), a smaller nonlinearity of $\mathcal{N}(E_g)$ (reduced slope) reflects the onset of the optical-field emission. For the 1-nm junction we obtain $n = 3.55$. In this situation, the potential barrier of the junction is lower and narrower and, as a consequence, the electron transfer involves both over-the-barrier transitions requiring at least four-photon absorption, and under-the-barrier tunneling transitions, dominated by three-photon absorption [see Fig. 4(b)]. A smaller number of absorbed photons (lower electron excitation energy, higher tunneling barrier) implies a too small tunneling exponent. The above analysis is supported by the TDDFT and model studies in Ref. [63], where the lightwave-induced transport in 1-nm and 2-nm junctions was addressed, albeit for somewhat different work function Φ.

To clearly identify the contribution of PAT to electron transport, the TDDFT results should reveal a change of the leading electron transport channel(s) when varying E_g. Indeed, consider the perturbative regime shown in Fig. 3(a). As follows from Eq. (1), the probability of absorbing ℓ photons scales as $\propto E_g^{2\ell}$. Obviously, for a very small E_g the lowest ℓ transport channel allowed by the symmetry (see below) will dominate. Increasing field strength in the gap leads to the involvement of higher-ℓ channels [64] for which the tunneling probability is higher. One might expect that the transition between dominant ℓ channels should then appear as a change of the slope in the log-log plot of $\mathcal{N}(E_g)$ [5,40,41]. Moreover, as follows from the semiclassical theory in Sec. II E, above certain E_g the tunneling regime of electron transport evolves into a regime dominated by over-the-barrier transitions. This change of the transport regime operates for parameter $\zeta = 1$ [see Eq. (24)], and it should also be evidenced by a change of the photon order n.

However, within the studied range of E_g, the TDDFT results for $d_{gap} = 1$ nm and $d_{gap} = 2$ nm feature linear log-log plot of $\mathcal{N}(E_g)$ with constant slope (except for the onset of the optically assisted tunneling). This can be explained by our semiclassical theory outlined in Secs. II D and II E. The ζ-parameter values $\zeta < 1$ do not allow reaching the perturbative regime of tunneling for these gap sizes within the studied range of E_g. The multiphoton regime of electron transport is then operative with an onset of the optical-field emission at $E_g \gtrsim 10$ V/nm. As follows from Eqs. (27) and (28), and in accord with TDDFT results, the photon order n in this situation is given by the threshold value $n = \frac{\mathcal{W}_{tb}}{\omega}$, where the tunneling barrier height $\mathcal{W}_{tb}$ is defined with Eq. (12). Reaching the perturbative regime at $\zeta \geqslant 1$ even with $d_{gap} = 1$ nm would require too low optical fields where $\mathcal{N}$ is then too small to be calculated with TDDFT.

To observe the change of the electron tunneling channels bringing the main contribution to PAT, one thus needs a smaller size of the gap which allows for sufficient tunneling probability at high electron binding energies. This is

confirmed in Fig. 4(a) by the results obtained for a narrow $d_{\rm gap} = 0.8$ nm gap where the change of the slope of the $\mathcal{N}(E_{\rm g})$ dependence clearly appears close to $E_{\rm g} \approx 3.5$ V/nm. The effective number of photons is $n \approx 2$ at lower $E_{\rm g}$. At higher $E_{\rm g}$ it is $n \approx 3$, close to the $\frac{\mathcal{W}_{\rm tb}}{\omega}$ threshold. It is tempting to associate the photon order n with the leading electron transfer channel $\ell_{\rm Main}$ where both two- and three-photon absorption are associated with the tunneling transition. Indeed, the electron energies of the $\ell = 2$ and $\ell = 3$ channels of PAT are below the potential barrier separating the nanowires as sketched in Fig. 4(b). In this respect, as we demonstrate below, the assignment of the leading electron transfer channel $\ell_{\rm Main}$ from effective photon order n should be done with care. This is because the $\mathcal{N} \propto E_{\rm g}^{2n}$ dependence generally stems from the simultaneous contribution of several electron transfer channels ℓ. It is only at lowest $E_{\rm g}$ values, in the perturbative regime, that the $n \simeq \ell_{\rm Main}$ link can be made. In this respect, $n \approx 3$ involves not only $\ell = 3$, but also higher ℓ channels corresponding to over the barrier transitions.

The evolution of the electron transport regime with $E_{\rm g}$ can be explained with the help of the SFT. For a junction width of 0.8 nm, the field amplitude $E_{\rm g} = 3$ V/nm results for the present system in $\zeta = 1$. As discussed in Sec. II E, the over-the-barrier electron excitation is not permitted within the semiclassical theory for field strengths below this value. In this situation, the electron transport can be described by the perturbative multiphoton regime of PAT. For $E_{\rm g}$ above this threshold, marked with a vertical red bar in Fig. 4(a), the over-the-barrier electron transport is possible. An effective photon order n quickly converges to $\frac{\overline{\mathcal{W}}_{\rm tb}}{\omega} \approx \frac{\mathcal{W}_{\rm tb}}{\omega}$, where the effective height $\overline{\mathcal{W}}_{\rm tb}$ of the tunneling barrier introduced in the semiclassical theory is defined with Eq. (23). The observed change in the slope of the $\mathcal{N}(E_{\rm g})$ dependence near $\zeta = 1$ thus signals a shift in the underlying transport channels.

Noteworthy, the TDDFT results in Fig. 4(a) do not show electron transfer associated with one-photon absorption as might be expected from the perturbative regime of PAT at low $E_{\rm g}$ and as reported in recent experiments [5,41]. At this point it is important to recall that a dc bias was applied to the junction in experimental conditions. For a symmetric junction at zero bias as considered here, the cw PAT theories predict zero net electron transfer [consider Eq. (1) for $U = 0$]. The rectification becomes possible owing to the single-cycle duration of the optical pulse, where the symmetry is broken by the optical field itself. The absence of PAT associated with one-photon absorption at low $E_{\rm g}$ can be then understood using perturbation theory, rotating-wave approximation, and the linear-response formalism as developed in Appendix C. We demonstrate that $\mathcal{N}$ is zero when driven by one-photon absorption in a symmetric system. The nonzero net electron transfer in the symmetric nanowire dimer requires at least a second-order process associated with two-photon absorption as we indeed observe in the TDDFT results.

This finding can be further illustrated with a one-dimensional single-active-electron model WPP study. In Fig. 5 we analyze the probability $\mathcal{P}_{L\to R}(\varphi)$ for an electron initially located in the left metal lead to be transferred across the $d_{\rm gap} = 0.8$ nm junction. Results of the WPP calculations for the single-cycle optical pulse with CEP $\varphi = 0$ (blue dots) and $\varphi = \pi$ (green dots) are shown as a function of the amplitude of the optical field in the gap $E_{\rm g}$. As follows from the fit of $\mathcal{P}_{L\to R}$ by the $E_{\rm g}^{2n}$ dependence, clear changes of n occur around $E_{\rm g} = 3$ V/nm ($\zeta = 1$), marked by a vertical gray bar. The underlying change of the transport regime is discussed in Sec. II E. At low $E_{\rm g} < 3$ V/nm ($\zeta > 1$), in the perturbative regime of PAT, electron transfer across the junction is dominated by one-photon absorption ($n = 1$ reflects the $\ell = 1$ channel of PAT). In this situation the effect of CEP is very small, in full accord with predictions of the first-order perturbation theory outlined in Appendix C. At high $E_{\rm g} > 3$ V/nm ($\zeta < 1$), below the onset of optical-field emission, nonlinearity increases ($n \approx 2.7$) and the results start to notably depend on CEP. This corresponds to the multiphoton regime with electron transport owing to PAT plus over-the-barrier transitions.

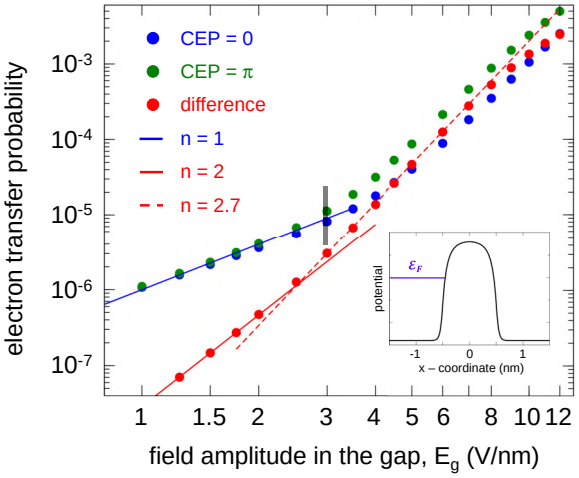

FIG. 5. Model 1D WPP study of electron transfer induced by the x-polarized single-cycle optical pulse ($\omega = 0.95$ eV, CEP $= 0$ and CEP $= \pi$) across metal leads separated by a 0.8-nm gap. The metal work function is $\Phi_{\rm M} = 5.0$ eV. Initially, an electron occupies an orbital at the Fermi energy $\mathcal{E}_F$ in the left lead. The electric field of the single-cycle pulse is given by Eq. (8). The probability $\mathcal{P}_{L\to R}$ of electron transfer from the left to the right electrode across the junction is shown with solid dots as a function of the field amplitude in the gap $E_{\rm g}$. Blue dots: $\mathcal{P}_{L\to R}(0)$ obtained with CEP $= 0$. Green dots: $\mathcal{P}_{L\to R}(\pi)$ obtained with CEP $= \pi$. Red dots show the difference $\mathcal{N} = \mathcal{P}_{L\to R}(\pi) - \mathcal{P}_{L\to R}(0)$ representing the net electron transfer induced by the CEP $= \pi$ single-cycle optical pulse between the two leads. Lines: fit by the $E_{\rm g}^{2n}$ dependence. The effective number of photons n is given in the legend. Clear changes of n occur around $E_{\rm g} = 3$ V/nm ($\zeta = 1$) marked by a vertical gray bar. The inset shows the dependence of the model potential in the gap region on the x coordinate. Energy zero corresponds to the vacuum level. For further details see the text.

The *net* electron transfer $\mathcal{N}$ (red dots) is given by the difference of electron transfer probabilities from one lead to the other. Using the symmetry of the system, one can write $\mathcal{N} = \mathcal{P}_{L\to R}(\pi) - \mathcal{P}_{R\to L}(\pi) = \mathcal{P}_{L\to R}(\pi) - \mathcal{P}_{L\to R}(0)$. Since for $E_{\rm g} < 3$ V/nm the one-photon absorption channels cancel each other, as explained above, the two-photon absorption ($n = 2$) determines the net electron transfer with $\mathcal{N} \propto E_{\rm g}^4$. This is followed by the transition to higher nonlinearity with $n = 2.7$ for $3 \lesssim E_{\rm g} \lesssim 8$ V/nm. Finally, upon

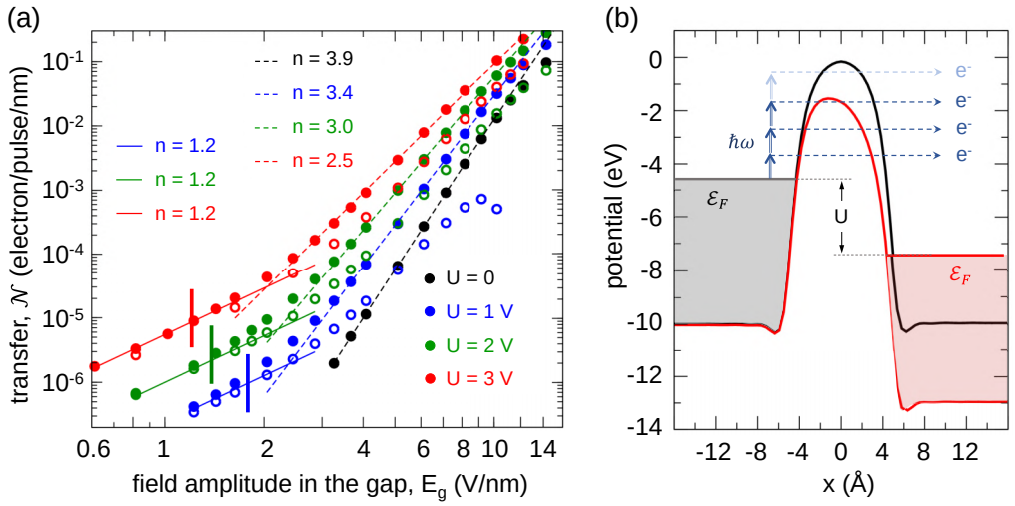

FIG. 6. Effect of an applied bias on electron transfer induced by a single-cycle x-polarized optical pulse ($\omega = 0.95$ eV, CEP $= 0$ and CEP $= \pi$), across a 1-nm-wide gap of a cylindrical nanowire dimer with work function $\Phi_M = 5.4$ eV. (a) Optically induced net electron transfer $\mathcal{N}$ calculated with TDDFT per pulse and per nm length of the dimer is shown as a function of the field in the gap E_g. Color dots: results obtained for different values of an applied dc bias U. Filled dots are used for CEP $= \pi$, and open dots of the same color are used for CEP $= 0$ except for $U = 0$ where only the CEP $= \pi$ result is shown. Lines: fit by the $\mathcal{N} \propto E_g^{2n}$ dependence characteristic for the multiphoton regime. The effective number of photons n is given in the legend. The vertical bars of the corresponding color mark the change of the transport regime at $\zeta = 1$. For further details see the legend. (b) One-electron potential in the 1-nm-gap region as a function of the x coordinate along the dimer axis. The energy is measured with respect to the vacuum level of the left cylinder. Black line: zero applied bias ($U = 0$); red line: applied bias $U = 3$ V as measured between the Fermi level energies of the nanowires indicated with $\mathcal{E}_F$. The effective work function $\Phi = 4.6$ eV is used in the TDDFT calculation (see Table I). The hatched areas indicate occupied electronic states of the valence band. Dashed horizontal arrows indicate electron tunneling and over-the-barrier transitions induced by ℓ-photon absorption. The latter is indicated with vertical arrows. Light color is used for $\ell = 4$-photon absorption with electron energy close to the top of the potential barrier, dominating transport in the $U = 0$ case.

further increase of E_g, the optical-field emission regime sets in, leading to lower nonlinearity. It is remarkable that the simple one-state single-electron model calculations capture the main trends of the calculated with TDDFT dependence of the net electron transfer on the optical field [see Fig. 4(a)].

B. Symmetry breaking by an applied bias

The $\ell = 1$ electron tunneling channel associated with one-photon absorption emerges in the net electron transfer for asymmetric systems. Such asymmetry occurs, e.g., in break junctions or STM tip-to-flat-surface junctions [101–103], as well as in junctions formed by different metals [104]. Symmetry breaking can also be controllably introduced by applying a dc bias across the junction [5,40,41]. For a dimer of identical parallel nanowires, we adopt the latter strategy, which enables direct comparison with recent experiments in tunneling junctions [5,40,41]. Along with breaking the symmetry, the applied bias in these experiments was used to vary the tunneling barrier and, consequently, the interplay between tunneling channels with different ℓ.

The effect of the applied bias U on the net electron transfer $\mathcal{N}$ induced by the single-cycle optical pulse across the 1-nm-wide gap is shown in Fig. 6(a). TDDFT calculations were performed for different values of the optical-field amplitude in the gap E_g. For zero bias and within the $\mathcal{N}$ range addressed here, we obtain a multiphoton character of the net electron transfer with an effective number of absorbed photons $n = 3.9$, close to Φ/ω. This indicates that overall, the electron transport is dominated by photoexcited electrons with energies close to the top of the potential barrier separating the metals [see Fig. 6(b)], in full agreement with the semiclassical theory (parameter $\zeta < 1$). Note that the slightly larger work function $\Phi_M = 5.4$ eV (also representative of gold) used here explains the somewhat larger n obtained for $U = 0$ when compared with the results reported for the 1-nm gap in Fig. 4.

The finite bias U applied across the gap reduces the potential barrier of the junction so that the net electron transfer increases. Moreover, the symmetry breaking introduced by the applied bias enables the contribution of electron tunneling assisted by one-photon absorption ($\ell = 1$ PAT channel) into $\mathcal{N}$. It follows from the TDDFT results in Fig. 6(a) that the one-photon absorption dominates for $E_g \lesssim 2.5$ V/nm with $\mathcal{N} \propto E_g^{2n}$ where $n \approx 1.2$. In agreement with the discussion in Sec. III A, the CEP dependence tends to be washed out in this situation. As predicted by the semiclassical theory and sketched in Fig. 3, with increasing E_g we observe the transition from the perturbative regime of PAT ($\zeta > 1$) dominated by the $\ell = 1$ channel to the multiphoton regime ($\zeta < 1$, PAT + ATI). The values of E_g corresponding to the parameter $\zeta = 1$, as introduced by our semiclassical theory, are marked in Fig. 6(a) by vertical color bars. The applied bias enhances the above-threshold ionization so that the transition shifts to lower E_g with increasing U.

In the multiphoton regime of electron transport ($E_g > 3$ V/nm), we obtain that the effective number of absorbed photons n is in the 2.5–3.4 range and it is approximately equal to $n \approx \mathcal{W}_{tb}/\omega$. Similar to the situation with $U = 0$, on average, the transferred electron energies approach the threshold value

determined by the height of the potential barrier of the junction $\mathcal{W}_{\rm tb}$ given by Eq. (14). The smaller n calculated for larger U reflects the reduction of the tunneling barrier by the applied bias [see Fig. 6(b)]. This result is fully consistent with the prediction of the SFT [Eq. (28)], and it was also reported in model calculations with simplified form of the potential barrier of the junction [60,105]. It is worth noting that in TDDFT we define the tunneling barrier height from the maximum of the self-consistent potential in the junction including the dc field owing to the applied bias [see Eq. (14)]. In the semiclassical theory, $\overline{\mathcal{W}}_{\rm tb}$ is determined by the average image potential [see Eq. (23)]. The dc field owing to the applied bias is accounted for via vector potential.

Notably, the TDDFT results reveal that only the transition from the one-photon $\ell = 1$ to the multiphoton regime of electron transport around $E_{\rm g} = 2.5$ V/nm is well marked. In the multiphoton regime, the contributions of individual transport channels ℓ cannot be resolved. With increasing $E_{\rm g}$, the effective photon order n, extracted from the power-law dependence of net electron transfer on the optical field $\mathcal{N} \propto E_{\rm g}^{2n}$, becomes an averaged characteristic. It rapidly converges to the threshold given by the height of the tunneling barrier in full accord with Eq. (28) of the semiclassical theory.

The degeneracy of the results obtained with CEP $= \pi$ and CEP $= 0$ at low $E_{\rm g}$, where one-photon absorption ($\ell = 1$ PAT channel) dominates electron transport, is lifted in the multiphoton regime at $E_{\rm g} > 3$ V/nm. Similar to the unbiased case, the net electron transport between parallel nanowires in the presence of a dc bias exhibits a sinusoidal dependence on the CEP. However, as reported earlier [62,63], and therefore not analyzed here, an applied bias leads to a vertical offset $\overline{\mathcal{N}}$, such that $\mathcal{N} \approx \mathcal{N}_0 \sin(\varphi - \pi/2) + \overline{\mathcal{N}}$. For a positive bias, for CEP $= \pi$, the optical and dc fields point in the same (negative) x direction, maximizing the net positive electron transport. For CEP $= 0$, the optical field is along the positive x direction, while the dc field points in the opposite direction, so that the net electron transport is close to minimum. The difference between the results for CEP $= \pi$ and CEP $= 0$ provides access to both the oscillation amplitude $\mathcal{N}_0$ and the offset $\overline{\mathcal{N}}$ of the CEP-dependent transport. Notably, at the lowest bias $U = 1$ eV, a strong optical field with CEP $= 0$ can reverse the direction of the net electron transfer. This is manifested in the $\mathcal{N}(E_{\rm g})$ dependence, which reaches a maximum at $E_{\rm g} \approx 9$ V/nm and changes sign at higher $E_{\rm g}$ (not shown in the log-log scale plot used here). For larger values of the applied bias, the net electron transfer is always from the left to the right cylinder because of the positive offset $\overline{\mathcal{N}}$ induced by U.

The suppression of PAT associated with the $\ell = 1$ single-photon channel with increasing gap size is illustrated in Fig. 7. The TDDFT calculations are performed for the 2-nm gap using an optical pulse with CEP $= \pi$. The applied bias U is set in such a way that the dc field in the junction $E_{\rm bias}$ is the same as for the 1-nm gap discussed in Fig. 6. Thus, the height of the tunneling barrier is similar in both cases. However, since the gap size increases from 1 nm to 2 nm the tunneling barrier broadens. This favors the multiphoton transitions with electron energies close to the threshold value $\mathcal{E}_F + \ell\omega \approx \mathcal{W}_{\rm tb}$. Small values of $E_{\rm g}$ are then required for the $\ell = 1$ channel to be observed. Consequently, the corresponding values of $\mathcal{N}$ would be extremely small, and lie outside the convergence

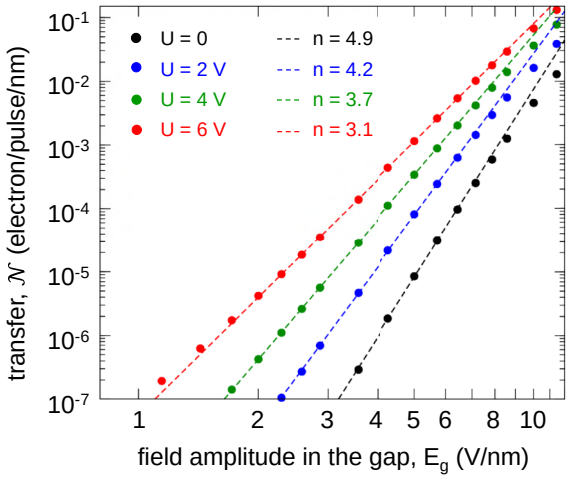

FIG. 7. Same as in Fig. 6(a), but for a 2-nm-wide junction. Only results obtained with CEP $= \pi$ are presented.

range of the present implementation of the TDDFT. Thus, the results in Fig. 7 reflect only the multiphoton regime of optically induced electron transport ($\zeta < 1$ in the semiclassical SFT) with an effective photon order n smaller for larger applied bias because of the smaller potential barrier. The suppression of below-the-barrier transitions also explains the overall higher n obtained for the 2-nm gap as compared to the 1-nm gap.

Additional insights into the interplay between electron tunneling channels associated with the absorption of different number of photons ℓ can be obtained from the analysis of the energy spectra of the transferred electron for a given initial state. To this end, we perform one-dimensional, one-electron WPP calculations (see Sec. II B) of electron transfer across a 1-nm gap between semi-infinite jellium metal leads. A bias $U = 2$ V is applied. The electron active in the optically assisted transitions initially occupies the orbital at the Fermi energy $\mathcal{E}_F$ in the left lead. To clearly resolve sidebands associated with the absorption of different numbers of photons ℓ in the energy spectra of the transmitted electron, we increase the optical pulse duration from 5.2 fs to 21 fs [$\tau = 3.4 \times 2\pi/\omega$, see Eq. (2)]. The WPP results are detailed in Fig. 8. It is worth noting that for a several-cycle pulse, such as that used here, the electron transport does not depend on CEP.

In Fig. 8(a), we show the dependence of the optically induced electron transfer on the amplitude of the optical field in the gap $E_{\rm g}$. Notice that although the WPP calculations address only the electron transfer from the left to the right lead, the results in Fig. 8 are representative of the net electron transfer. Indeed, for $U = 2$ eV the electron transfer in the opposite direction (from the right lead to the left lead) would require absorption of at least two additional photons and is therefore essentially smaller under the present conditions. Similar to the findings in Sec. III A, comparison of the TDDFT results in Fig. 6 with the WPP results in Fig. 8(a) shows that the one-dimensional single-active-electron model reproduces the trends obtained in TDDFT calculations with an applied bias. The WPP results are also consistent with an analysis based on the semianalytical theory (see Ref. [64] and

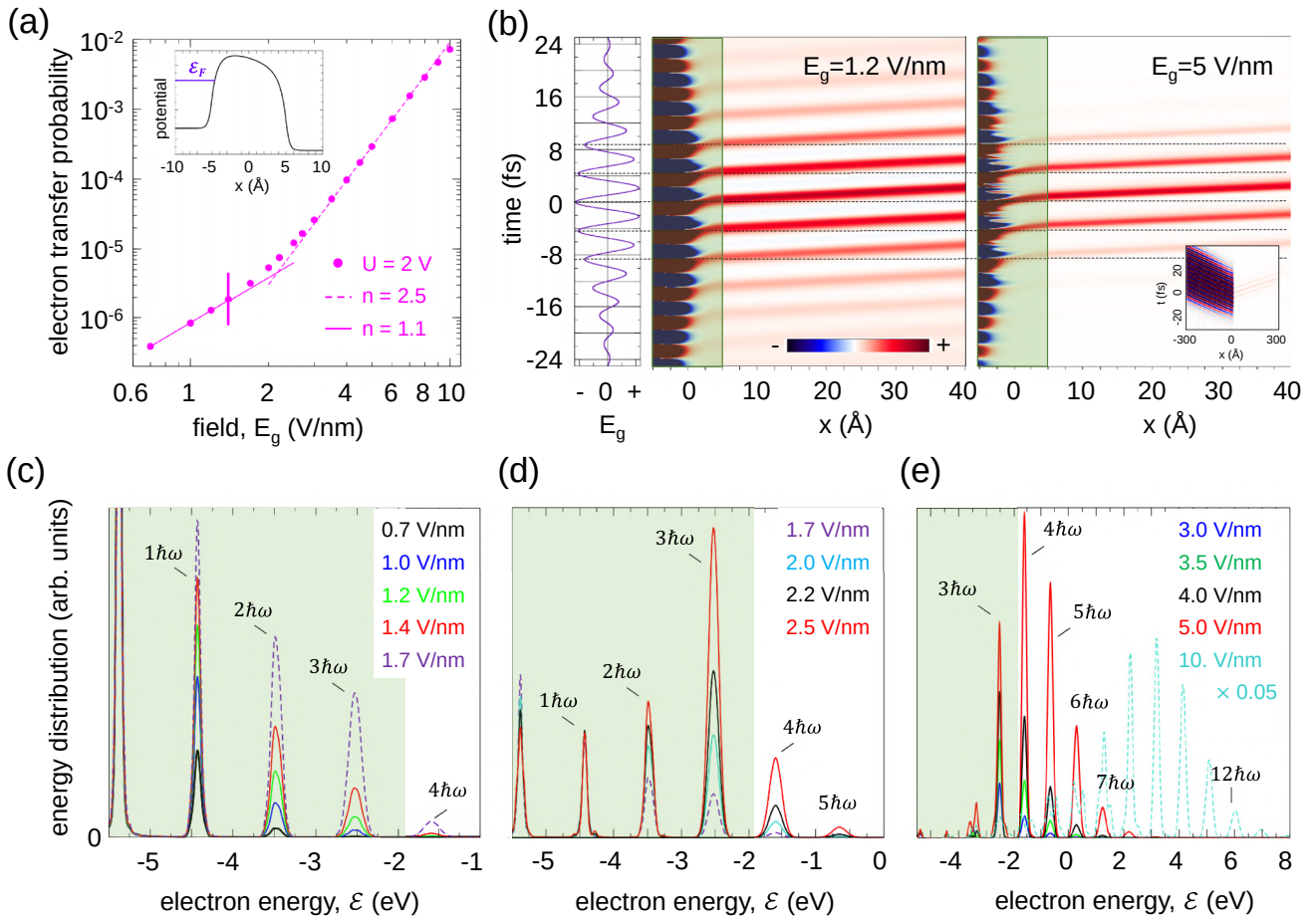

FIG. 8. Model 1D WPP study of the optically induced electron transfer between metal leads separated by a 1-nm vacuum gap. Metal work function $\Phi_M = 5.4$ eV. A dc bias $U = 2$ V is applied across the gap. The electric field of the several-cycle optical pulse is given by Eq. (8) with $\tau = 3.4 \times 2\pi/\omega$, and CEP $= \pi$. (a) Probability of optically induced electron transfer (for this duration of the optical pulse it is independent of CEP) as a function of the optical-field amplitude in the gap E_g. Initially, the active electron occupies an orbital with Fermi energy $\mathcal{E}_F$ in the left lead. WPP results are shown with solid dots. The vertical bar marks $\zeta = 1$. The lines display the fit by the E_g^{2n} dependence. The effective number of photons n is given in the legend. The inset shows the x-coordinate dependence of the model potential in the gap region. Energy zero corresponds to the vacuum level of the left lead. (b) 2D maps of the normalized electron probability current density $j_{opt}(x, t)$ induced by an optical pulse with $E_g = 1.2$ V/nm (left subpanel), and with $E_g = 5$ V/nm (right subpanel), as indicated in the legends. The WPP results are shown as a function of the x coordinate (horizontal axis) and time (vertical axis). The color code is given in the inset of the left subpanel. The line plot at the left shows the time evolution of the electric field in the gap. The shaded green region of x coordinates indicates the junction. The dashed lines mark the crests of the field in the gap with negative polarity. The inset of the right subpanel shows the 2D map of $j_{opt}(x, t)$ using large x scale. (c)–(e) Energy spectra of the electron transferred across the gap into the right lead calculated for different E_g as indicated in the legends. Results are shown as a function of electron energy $\mathcal{E}$ measured with respect to the vacuum level of the left lead. In (e) results for $E_g = 10$ V/nm are scaled by $\times 0.05$. The shaded green region indicates electron energies which are below the barrier of the junction, and therefore correspond to tunneling transitions. For further details see the text.

Sec. II D). Specifically, at low E_g ($\zeta > 1$), photon-assisted electron transport is dominated by one-photon absorption ($n = 1.1$), whereas for $E_g \gtrsim 3$ V/nm ($\zeta < 1$) a higher nonlinearity characteristic for the multiphoton regime sets in. In this regime, an effective number of absorbed photons quickly converges to $n = 2.5$, close to the tunneling barrier threshold $\mathcal{W}_{tb}/\omega = 2.7$, and remains essentially constant with increasing E_g up to the onset of the optical-field emission.

In Fig. 8(b) we show the electron probability current density $j_{opt}(x, t)$ induced by the optical pulse. The WPP results reveal electron bursts emitted from the surface of the left lead at the crests of the optical field with negative polarity. These bursts traverse the junction (hatched green area) in less than 1 fs, and are subsequently injected into the right lead. Since the optical and dc fields are screened inside the metal, the injected electron follows a straight-line trajectory after crossing the metal-vacuum interface of the right lead. Under the present conditions, the applied bias and narrow junction impede the quiver motion that would reverse the direction of electron propagation in the gap (see also Ref. [63]).

The stronger nonlinearity of electron transport with electric-field strength in the gap or, equivalently, the larger effective number of absorbed photons in the multiphoton regime, results in a shorter time interval during which the optical pulse drives the transport between the leads. This is evidenced in Fig. 8(b) by the reduced number of electron bursts

emitted at the crests of the optical field and traversing the junction for $E_g \gtrsim 5$ V/nm (multiphoton regime) compared to the data obtained for $E_g \gtrsim 1.2$ V/nm (tunneling dominated by one-photon absorption). Importantly, in all cases considered, we find that the optically induced electron transfer dynamics instantaneously follows the temporal variation of the optical field. The probability current density $j_{opt}(x,t)$ in the gap region is nonzero only while the optical pulse acts on the system. This result is in full agreement with previous TDDFT and one-electron studies of electron transport in metallic gaps and photoemission from metal surfaces driven by single-cycle and longer laser pulses [24,56–64]. It highlights the contribution of a fast, one-step process in which electron excitation by the laser pulse and transport across the gap cannot be separated in time.

It is also worth noting that, because of optical-field screening inside the metal and electron momentum change at the jellium surface, electron excitation occurs within the surface layer (analogous to the Landau damping mechanism of surface plasmons [46]). A fraction of the excited electrons crosses the gap, leading to electron transport between the leads. However, the majority remains within the "parent" left lead, propagating from the surface into the bulk, as evidenced by the inset of the right subpanel of Fig. 8(b). In the TDDFT calculations we obtain qualitatively similar trends. However, because of contributions from both surfaces across the junction, and because of the overlap between current densities associated with the electron transport and those arising from polarization of the cylinders, the data are considerably more difficult to analyze [63]. The relaxation of the nonequilibrium carriers generated at the surface and propagating into the bulk involves electron-electron and electron-phonon scattering events [20,44–46,106–108], which are not included in the one-electron WPP calculations and lie beyond the ALDA-TDDFT framework employed here [109–111].

Finally, in Figs. 8(c)–8(e) we show the energy spectra of the transferred electron given by the energy-resolved outgoing electron probability current density in the asymptotic region inside the right lead $j(x \to \infty, \mathcal{E})$. Results are obtained for different values of the optical field in the gap. The electron energy $\mathcal{E}$ is measured with respect to the vacuum level of the left lead. The spectra display peaks at energies $\mathcal{E}_F + \ell\omega$ corresponding to electron transfer assisted by absorption of ℓ photons. For optical fields $E_g \lesssim 1.4$ V/nm [Fig. 8(c)], the $\ell = 0, 1, 2, 3$ contributions are visible. Electron transfer occurs primarily via tunneling with electron energies below the potential barrier of the junction (the corresponding energy range is indicated by the hatched green area in Figs. 8(c)–8(e). The intensity of the sidebands scales as $\propto E_g^{2\ell}$ with the $\ell = 0$ peak (dc tunneling) and the $\ell = 1$ peak (tunneling assisted by one-photon absorption, i.e., the $\ell = 1$ channel of PAT) dominating the spectrum. These results fully agree with WPP results reported in Fig. 8(a) for this range of E_g. Indeed, the effective photon order $n = 1.1$ obtained using fit by $\mathcal{N} \propto E_g^{2n}$ dependence corresponds to the $\ell = 1$ channel leading the PAT.

The electron energy spectra in Fig. 8(c) shed light on why, in Fig. 8(a), the theoretical parameter $\zeta = 1$, indicating a change of the transport regime, appears at smaller E_g than the transition from lower ($n = 1$) to higher ($n = 2.5$) nonlinearity in the simulated $\mathcal{N}$. Similar trends are observed in Figs. 4(a), 5, and 6(a). According to the definition of the cutoff energy in Eq. (30), the condition $\zeta = 1$ (here at $E_g \sim 1.4$ V/nm) corresponds to the point where $\mathcal{E}_{cutoff}$ reaches the barrier threshold, so that at higher E_g electronic states above the potential barrier can be populated. As shown in Fig. 8(c), clear evidence of photon-assisted excitation above the barrier emerges only when $E_g > 1.4$ V/nm. Because the contribution of high-energy sidebands near the cutoff is statistically small, a larger field strength is required to increase n and, in particular, to reverse the perturbative evolution of the sideband weights with ℓ.

This change in the ℓ progression of the sidebands is clearly observed in Fig. 8(d) for 1.7 V/nm $\leqslant E_g \leqslant$ 2.5 V/nm. The sequence evolves from the decreasing perturbative $E_g^{2\ell}$ trend described by Eq. (1) to a reversed progression with dominance of the three-photon absorption process ($\ell = 3$ channel of PAT). The electron energies corresponding to the $\ell = 1, 2, 3$ PAT channels are below the top of the potential barrier, so that the tunneling transitions continue to dominate the transport. Note that within this range of E_g, the nonlinearity of the $\mathcal{N}(E_g)$ dependence progressively increases. For higher fields [Fig. 8(e)], the leading contributions to the energy spectrum shift to the $\ell = 4, 5$ sidebands. For $E_g \geqslant 5$ V/nm electron transport becomes dominated by classically allowed over-the-barrier transitions. At the onset of the optical-field emission regime ($E_g = 10$ V/nm), photon orders up to $\ell = 12$ can be clearly observed, with electron energies reaching up to 7 eV above the barrier [theoretical cutoff is 7.63 eV according to Eq. (30)].

To summarize the results obtained in this section, TDDFT calculations show, in agreement with semiclassical theory, that establishing a one-to-one correspondence between the dominant channel ℓ_{Main} of optically induced transport and the effective photon order n extracted from the $\mathcal{N} \propto E_g^{2n}$ dependence must be done with care. Strictly speaking, assignment is only possible in the limit $E_g \to 0$, where n match the lowest possible ℓ. In this regime, one can resolve one-photon-assisted tunneling ($\ell = 1$) for nonsymmetric junctions, and the two-photon-assisted tunneling ($\ell = 2$) for symmetric junctions. In the multiphoton regime of electron transport, the contributions of higher-photon orders overlap. The transition between the leading transport channels ℓ_{Main} with changing E_g cannot be resolved. The effective photon order n then represents an average characteristic. With increasing E_g, it quickly converges to the threshold value set by the barrier height $n \approx \mathcal{W}_{tb}/\omega$. This behavior contrasts with photoemission into vacuum, as in the case of an individual surface or wide junction between metals, where PAT with electron energies below the barrier is suppressed. In this situation, the E_g^{2n} dependence of electron emission or transport over the entire E_g range prior to the onset of the optical-field emission, is determined by $n \approx \Phi_M/\omega$ corresponding to the multiphoton photoemission threshold.

IV. COMPARISON WITH AVAILABLE EXPERIMENTAL DATA

A number of recent experiments reported on the effect of an applied bias and of the strength of the optical field on lightwave-driven electron tunneling in metallic junctions [5,9,40–42,49,74,112,113]. In particular, the relative

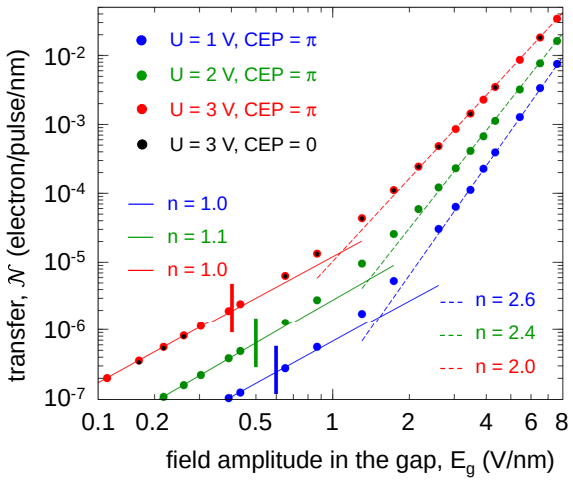

FIG. 9. Effect of an applied dc bias on electron transfer induced by a 7-fs-long x-polarized optical pulse [$\tau = 4.2$ fs, $\omega = 1.6$ eV, CEP $= 0$ and CEP $= \pi$ in Eq. (2)] across a 1-nm-wide gap of a nanowire dimer. The work function is $\Phi_M = 5.3$ eV. Dots: optically induced net electron transfer $\mathcal{N}$ calculated with TDDFT per pulse and per nm length of the dimer as a function of the field in the gap E_g. The different colors indicate different values of the applied dc bias U and CEP, as explained in the legend. Lines: fit by the $\mathcal{N} \propto E_g^{2n}$ dependence. The effective number of photons n is given in the legend. The vertical bars of the corresponding color mark the transport regime change at $\zeta = 1$.

contributions of tunneling channels involving single-photon and multiphoton absorption have been examined [5,40,41]. The interpretation of these experiments typically involves parametrization of the electron excitation and tunneling processes. To gain clarity in the underlying physical mechanisms it is thus of interest to examine the TDDFT results for experimentally studied systems.

A. Gold bowtie antenna

The contributions of one-photon- and multiphoton-assisted tunneling in the gap of a gold bowtie antenna were investigated by Luo and collaborators [5]. In their experiment, electron transport across the gap was induced by 7-fs laser pulses, resonant with the nanoantenna plasmon at $\omega = 1.6$ eV. The radii of the nanoantenna tips forming the gap were estimated to be 5 nm. Since this matches the radii of the metallic nanowires used in our calculations, a comparison of the experimental data with TDDFT calculations becomes particularly relevant.

In Fig. 9 we show the net electron transfer $\mathcal{N}$ across the gap of a nanowire dimer calculated with TDDFT as a function of the optical-field strength in the gap E_g for different values of the applied bias U. Following the discussion of experimental results in Ref. [5], we consider a gap of 1 nm and a metal work function $\Phi_M = 5.3$ eV representative of gold. The incident optical pulse is described by Eq. (2) with $\omega = 1.6$ eV and $\tau = 4.2$ fs (corresponding to an intensity FWHM of 7 fs). In contrast to the single-cycle optical pulse addressed in the previous section, the several-cycle pulse used here results in a negligible dependence of $\mathcal{N}$ on CEP. This is illustrated in Fig. 9 were calculations performed for an applied dc bias $U = 3$ V are shown for CEP $= \pi$ (red dots) and CEP $= 0$ (black dots).

Qualitatively, the results reported in Fig. 9 are similar to those discussed in Fig. 6(a). For small E_g, optically induced electron transport is dominated by single-photon absorption. The multiphoton absorption prevails for $E_g \gtrsim 1.5$ V/nm. A higher applied bias U lowers the potential barrier between the nanowires so that $\mathcal{N}$ becomes larger over the entire E_g range. For the same reason, in the multiphoton regime, the effective number of photons n driving the transport decreases with increasing U. Note that the fundamental frequency $\omega = 1.6$ eV corresponding to the experiment of Luo *et al.* [5] is used here, whereas the results in Fig. 6(a) are obtained with $\omega = 0.95$ eV. The difference in photon energy accounts for the different effective photon orders n obtained in the two sets of results. In line with experimental findings [5], for an applied bias of $U = 3$ V we find the following:

(1) The optically assisted electron tunneling with $\ell = 1$ photon absorption at low E_g evolves into a multiphoton regime with effective photon order $n = 2$ as E_g increases;

(2) No higher-order nonlinearity $n > 2$ is observed over a wide range of optical-field strengths in the gap, up to the onset of the optical-field emission regime, which occurs at $E_g \approx 12$ V/nm (not shown).

According to the SFT, TDDFT, and model WPP calculations performed in Sec. III (see Fig. 8), the second finding implies that while several ℓ channels (photon absorption orders) contribute to electron transport in the multiphoton regime, the overall net electron transfer follows a scaling $\mathcal{N} \propto E_g^{2n}$ with $n = 2$. This effective number of photons n is given by the threshold for over-the-barrier transitions $n \approx \mathcal{W}_{tb}/\omega$. It remains constant with increasing E_g up to the onset of the optical-field emission regime, in agreement with Eqs. (27) and (28).

For an applied bias $U = 3$ V, a clear change of the effective photon order n from the one-photon to the multiphoton regime occurs in the TDDFT calculations for $E_g \approx 1$ V/nm. In the experiment [5], under the same bias, this transition is observed for a free-space electric field of ≈0.09 V/nm. The theory is consistent with experiment when considering that the field enhancement due to the plasmon excitation in the gap of the actual device is of the order of $\mathcal{R} = 10$. This enhancement is smaller than that predicted by classical electrodynamics simulations [5]. However, for 1-nm gaps, quantum effects such as nonlocality become significant [114,115], so that classical results should be taken with caution.

In the experiment, the transition between the two regimes corresponds to a current of 20–30 pA, i.e., to approximately two electrons transferred per pulse. Considering that the experimental device contains a parallel circuit of seven bowtie antennas, each 30 nm in height, this translates to about 10^{-2} electrons transferred per pulse and per nanometer of antenna height, approximately three orders of magnitude higher than the TDDFT prediction. One of the reasons behind this discrepancy is that, because of plasmon ringing, the effective duration of the optical pulse in the gap of the experimental antenna is about twice as long as that in free space [5]. This effect is not captured in the TDDFT simulations because of the use of a free-electron metal model and a simplified

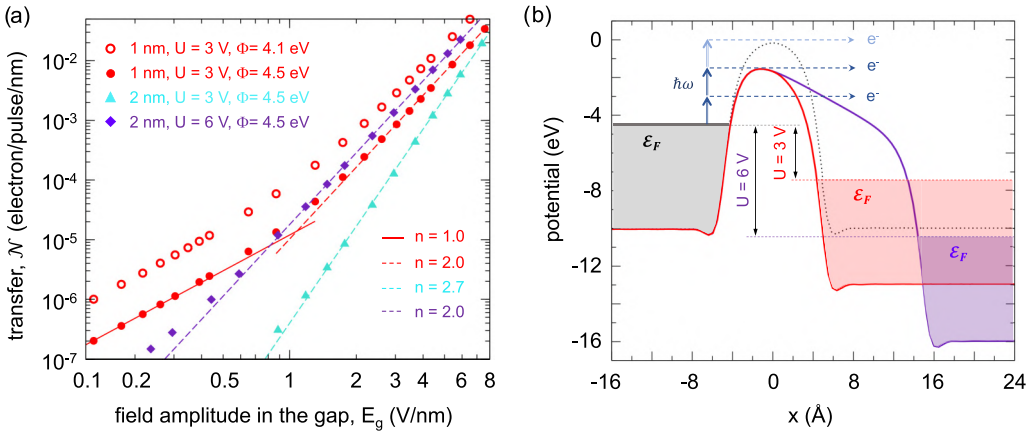

FIG. 10. Effect of the work function Φ, gap size $d_{\rm gap}$, and applied bias U on the electron transfer induced by a 7-fs-long x-polarized optical pulse [$\tau = 4.2$ fs, $\omega = 1.6$ eV in Eq. (2)] across the gap of a nanowire dimer. (a) Symbols show the net optically induced electron transfer $\mathcal{N}$ calculated with TDDFT per pulse and per nm length of the dimer as a function of the field in the gap $E_{\rm g}$. Calculations are performed for different values of Φ, $d_{\rm gap}$, and U as explained in the legend. The lines display the fit by the $\mathcal{N} \propto E_{\rm g}^{2n}$ dependence. The effective number of photons n is given in the legend. (b) One-electron potential in the gap region as a function of x coordinate along the dimer axis. The energy is measured with respect to the vacuum level of the left cylinder. Black dotted line: $d_{\rm gap} = 1$ nm, $U = 0$ V; red line: $d_{\rm gap} = 1$ nm, $U = 3$ V; violet line: $d_{\rm gap} = 2$ nm, $U = 6$ V. The applied bias is measured between the Fermi levels $\mathcal{E}_F$ of the metal nanowires. The hatched areas indicate occupied electronic states of the valence band. The dashed horizontal arrows indicate electron tunneling and over-the-barrier transitions induced by ℓ-photon absorption (vertical solid arrows). Light color is used for the $\ell = 3$-photon absorption with electron energy close to the top of the potential barrier dominating transport in the $U = 0$ case.

geometry with the plasmon mode off resonance with the optical frequency, as discussed in Sec. II. An approximate account for plasmon ringing through scaling the calculated net electron transfer $\mathcal{N}$ by a factor of 2 does not change the substantial difference between the experimental and our theoretical results.

Along with the pulse duration, the discrepancy between theory and experiment may also stem from differences in the optical transitions of the free-electron metal used in the present TDDFT calculations and of the actual gold studied experimentally. In addition to possible band-structure effects, there is also uncertainty in the geometry of the actual experimental device, particularly in the gap size, as acknowledged by Luo *et al.* [5], as well as in the work function of the nanoantennas. These last two factors strongly affect the electron tunneling and, consequently, the net electron transfer.

In Fig. 10, we explicitly address the effect of gap size and metal work function on electron transport in the system. One can use Table I to relate the work function Φ used in the ALDA TDDFT and the actual work function $\Phi_{\rm M}$ of the metals across the gap that the theory is designed to represent. When the gap size changes from 1 nm to 2 nm at fixed U and fixed Φ, the tunneling barrier becomes broader and higher. Consequently, the effective photon order n increases, and the net electron transfer $\mathcal{N}$ drops off by several orders of magnitude, in particular at low $E_{\rm g}$ [compare filled red circles and light blue triangles in Fig. 10(a)]. The dropoff of the tunneling probability is most pronounced for electrons with high binding energies, rendering the $\ell = 1$ PAT channel undetectable within the computed $\mathcal{N}$ range.

As an interesting observation, if a bias $U = 6$ V is applied across the 2-nm gap, the dc field in the gap is identical to that in the 1-nm gap under an applied bias of $U = 3$ V. The tunneling barrier then has the same height for both gap sizes. However, for electrons with $\mathcal{E}_{\rm F} + \omega$ energies, the width of the tunneling barrier is larger for $d_{\rm gap} = 2$ nm [see Fig. 10(b)]. As a result, while in the multiphoton regime the effective $n = 2$ is the same for both cases, the one-photon PAT channel at low $E_{\rm g}$ is observed clearly only for $d_{\rm gap} = 1$ nm, while for the 2-nm gap it becomes marginally distinguishable at very low $\mathcal{N}$ [compare violet diamonds and filled red circles in Fig. 10(a)].

Similarly to the pronounced effect of changing the gap size, a reduction of the work function from $\Phi = 4.5$ eV to 4.1 eV leads to an order of magnitude increase in the net electron transfer [compare filled and open red circles in Fig. 10(a)]. This brings our theoretical results closer to the experiment [5]. Given experimental uncertainties, in particular concerning essential parameters such as gap geometry and work function, we consider that the qualitative agreement between theory and experiment is sound. It is worth noting that since in the multiphoton regime the nonlinearity of the $\mathcal{N}(E_{\rm g})$ dependence is the same in theory and experiment ($n = 2$), the height of the tunneling barrier should be captured reasonably well in our calculations.

We close our comparison with the experiment by Luo *et al.* [5] by showing in Fig. 11 the calculated dependence of the net electron transfer $\mathcal{N}$ on the applied bias U for three representative values of the amplitude of the optical field in the gap: $E_{\rm g} = 0.4$ V/nm corresponding to the one-photon absorption regime of electron transfer, $E_{\rm g} = 2.2$ V/nm corresponding to the multiphoton regime, and $E_{\rm g} = 1.3$ V/nm near the transition between these two regimes. For $E_{\rm g} = 0.4$ V/nm and $E_{\rm g} = 1.3$ V/nm the results are normalized by a scaling factor $X = \mathcal{N}_{E_{\rm g}}(U)/\mathcal{N}_{E_{\rm ref}}(U)$, where $E_{\rm ref} = 2.2$ V/nm and $U = 3$ V. We find that the overall shape of the $\mathcal{N}(U)$ dependence is only weakly sensitive to $E_{\rm g}$, and it closely resembles the experimental data [see Fig. 4(a) in Ref. [5]].

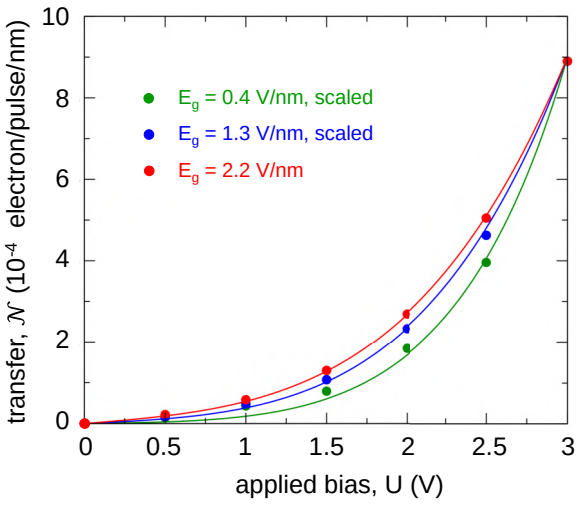

FIG. 11. Effect of an applied bias on optically induced electron transfer across a 1-nm gap between metal cylinders with work function $\Phi_M = 4.9$ eV (see also open red circles in Fig. 10). Results are shown for three values of the optical field in the gap 0.4, 1.3, and 2.2 V/nm as displayed in the legend. Dots: net optically induced electron transfer $\mathcal{N}$ calculated with TDDFT per pulse and per nm length of the dimer as a function of an applied bias U. The x-polarized optical pulse has 7-fs duration and $\omega = 1.6$ eV. The results for $E_g = 0.4$ V/nm and $E_g = 1.3$ V/nm are scaled to match $\mathcal{N}$ calculated for $E_g = 2.2$ V/nm, and $U = 3$ V. Solid lines of the corresponding color: results obtained within the semiclassical SFT framework and scaled to match the $\mathcal{N}$ calculated with TDDFT for $E_g = 2.2$ V/nm, and $U = 3$ V. See the text for further details.

This behavior can be explained using the SFT framework. Since the field amplitudes E_g considered here roughly satisfy $\zeta > 1$ and $\gamma \gg 1$, the multiphoton photoemission described by Eqs. (27) and (28), and in a more precise form by Eq. (B9), becomes applicable. Taking into account the symmetry of the system, the net electron transfer can be analytically expressed as

$$\begin{aligned}\mathcal{N}(U) &= \mathcal{P}_{L\to R}(U) - \mathcal{P}_{R\to L}(U) \\ &= \mathcal{P}_{L\to R}(U) - \mathcal{P}_{L\to R}(-U),\end{aligned} \tag{31}$$

where $\mathcal{P}_{L\to R}(U)$ can be obtained from Eq. (B9) with $E_{\rm bias} = U/d_{\rm gap}$, and using $\mathcal{W}_{\rm tb} \approx \Phi$. Importantly, considering the leading power-law dependence of the transition probability on the optical field [Eq. (28)], the photon number n is independent of E_g, which explains the weak sensitivity of the shape of $\mathcal{N}(U)$ to variations in E_g. For comparison, we normalize in Fig. 11 the SFT results such that for $U = 3$ V all the results coincide with the value of $\mathcal{N}$ calculated with TDDFT for $E_g = 2.2$ V/nm.

B. Tunneling junction between silver surfaces

Finally, we apply our approach to study electron transport induced by a several-cycle optical pulse with carrier frequency $\omega = 2.33$ eV and a duration of 6 fs. The sufficiently long pulse duration ensures that the net electron transfer $\mathcal{N}$ is independent of the CEP, similarly to the behavior discussed in Sec. IV A. We use a typical work function of silver $\Phi_M = 4.5$ eV [98] with the aim of comparing the present results with recent cw experiments performed by Lin and collaborators [41], who studied multiphoton photocurrents in a STM junction between a silver tip and an Ag(111) surface. Similar experiments involving gold tip and Cu(100) surface have been conducted by Schröder *et al.* [40]. The authors of Ref. [41] argued that the band structure of Ag(111) has no effect on the lightwave-induced electron transport, which supports the applicability of the free-electron model in this case. We further comment on the validity and limitations of this approximation below. It is worth noting that the STM junction between the tip and the surface is nonsymmetric. However, an applied bias used in experiments overrides the effect of the symmetry break because of the geometry [41]. This validates the symmetric junction geometry used in our calculations, provided a dc bias is applied as the main source of asymmetry.

The different panels in Fig. 12 show the net electron transfer $\mathcal{N}$ calculated as a function of optical-field amplitude in the gap E_g, applied bias U, and gap size $d_{\rm gap}$. To facilitate comparison with experiment, we adopt the form of the data analysis used in the experimental work [41]. The dependence of $\mathcal{N}$ on E_g for several values of U [Fig. 12(a)], and the dependence of the effective photon order n on U for several values of E_g [Fig. 12(b)] are calculated for a fixed size of the gap $d_{\rm gap} = 1.6$ nm, consistent with the experimental configuration [41].

The theoretical results reported in Fig. 12(a) are in qualitative agreement with experiment and can be interpreted using the general trends of optically assisted electron transfer discussed above and in Ref. [64]. Thus, because of the relatively large gap width, tunneling is suppressed at low bias, and electron transport is dominated by electrons excited above the barrier. The effective number of absorbed photons $n = 2$ is therefore set by the energy threshold for the multiphoton process $n = \Phi/\omega$. Increasing U lowers the potential barrier, leading to the progressive emergence of the $\ell = 1$ one-photon-assisted tunneling channel for small $E_g \lesssim 1.5$ V/nm. In this range of E_g, the interplay between the $\ell = 1$ and higher-order transport channels manifests itself in a gradual decrease of the observed nonlinearity n with increasing bias. Ultimately, $n = 1$ is reached for $U = 3$ V and for $U = 3.5$ V. Above $E_g \approx 1.5$ V/nm, the multiphoton regime persists due to the significant contribution of $\ell > 1$ channels, albeit the effective photon order n is somewhat reduced for large U.

The effective local (with respect to E_g) photon order n is shown in Fig. 12(b) as a function of the applied bias for several E_g. The field amplitudes E_g used here for the TDDFT calculations match the field amplitudes in the junction within the 0.2–0.9 V/nm range as we obtained from the near-field intensity estimations performed by Lin and collaborators [41], who accounted for the plasmon enhancement in the system. The effective local photon order n is obtained via numerical differentiation of the $\mathcal{N}(E_g)$ curve at fixed bias U according to $n = \frac{E_g}{2\mathcal{N}(E_g)} \frac{\partial \mathcal{N}(E_g)}{\partial E_g}$. The results in Fig. 12(b) reflect the transition from the multiphoton-dominated transport to one-photon-assisted tunneling ($\ell = 1$) due to the reduction of the tunneling barrier by the applied bias. This transition is more abrupt for low E_g since weak optical fields favor lower photon-order processes (recall the $E_g^{2\ell}$ scaling of different

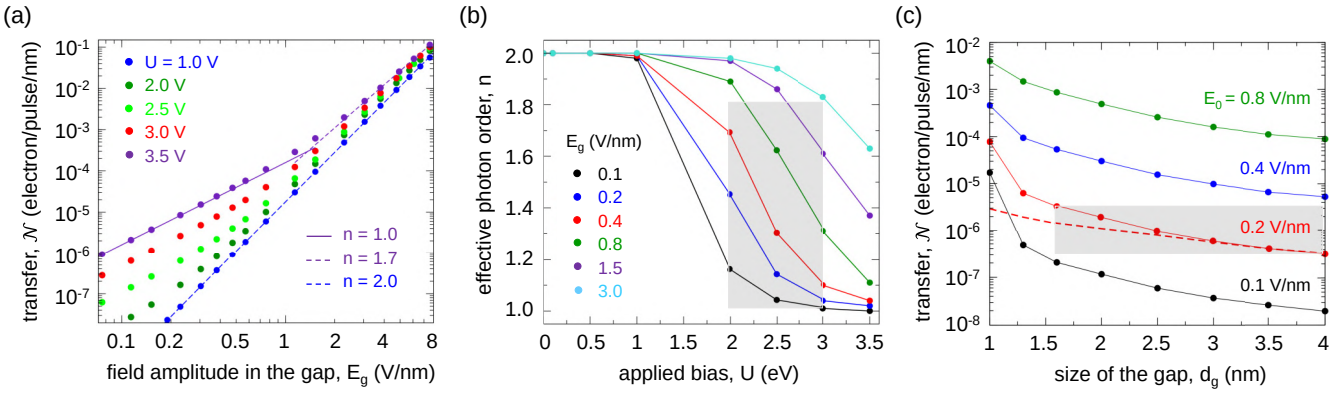

FIG. 12. Effect of an applied bias U and gap size $d_{\rm gap}$ on optically induced electron transfer across the gap of the nanowire dimer. The several-cycle x-polarized optical pulse is 6 fs long [$\tau = 3.6$ fs, and $\omega = 2.33$ eV in Eq. (2)]. The TDDFT calculations are performed with CEP $= \pi$. Notice, however, that for this several-cycle pulse, results are independent of CEP. In all the panels, results are shown per pulse and per nm length of the dimer. (a) Gap size $d_{\rm gap} = 1.6$ nm. Dots: Optically induced net electron transfer $\mathcal{N}$ calculated with TDDFT as a function of the field in the gap E_g for different values of the applied dc bias U. Lines: Fit by the $\mathcal{N} \propto E_g^{2n}$ dependence, where n is the effective number of absorbed photons. For further details see the legend. (b) Gap size $d_{\rm gap} = 1.6$ nm. Lines with dots: Effective local photon order (effective number of photons driving the transport for a given E_g) defined from the $\mathcal{N}(E_g)$ calculated with TDDFT as $n = \frac{E_g}{2\mathcal{N}(E_g)} \frac{\partial \mathcal{N}(E_g)}{\partial E_g}$. Results are shown as a function of the applied dc bias U for different values of the optical-field amplitude in the gap E_g as indicated in the legend. The gray shaded region indicates the typical variation range of $\mathcal{N}$ with U obtained experimentally [41]. (c) Applied dc bias $U = 0.5$ V. Lines with dots: Optically induced net electron transfer $\mathcal{N}$ calculated with TDDFT as a function of gap size $d_{\rm gap}$ for different values of the amplitude of the incident optical field E_0 as indicated in the legend. The amplitude of the optical field in the gap is $E_g = \mathcal{R}E_0$, where the field enhancement $\mathcal{R}$ depends on $d_{\rm gap}$ (e.g., $\mathcal{R} = 3.0$ for $d_{\rm gap} = 1.6$ nm). Dashed red line: fit by the $\mathcal{R}^4$ dependence expected for electron transport driven by two-photon absorption. The gray shaded region indicates the typical variation range of $\mathcal{N}$ with $d_{\rm gap}$ obtained experimentally [41].

ℓ channels at low optical fields). Overall, we find that the present calculations reproduce the typical variation range of $\mathcal{N}$ with U reported experimentally [41] and indicated with the gray shaded region.

In Fig. 12(c), we study the evolution of the lightwave-induced electron transport with gap size $d_{\rm gap}$. For the sake of comparison with the experimental data [41], we show the results as a function of the free-space field amplitude E_0. For the same reason, we performed the TDDFT calculations using relatively low applied bias ($U = 0.5$ eV), such that the tunneling barrier is only weakly affected by the dc field. Under these conditions, the evolution of the dc tunneling current with junction size can be estimated as $\propto \exp(-2\sqrt{2\Phi_{\rm M} - U}\, d_{\rm gap})$. According to this estimate, the dc tunneling current decreases by an order of magnitude when $d_{\rm gap}$ increases by 1 Å (0.1 nm). Therefore, within the $d_{\rm gap}$ range shown in Fig. 12(c), the lightwave-induced current dominates electron transport in the system [40,41]. Because of the reduction of the tunneling barrier for optically excited electrons, the contribution of the $\ell = 1$ PAT channel associated with one-photon absorption decays more slowly with increasing junction size. It follows the $\propto \exp(-2\sqrt{2(\Phi_{\rm M} - \omega) - U}\, d_{\rm gap})$ dependence, which is indeed observed in Fig. 12(c), for the lowest E_0 and for 1 nm $\leqslant d_{\rm gap} \leqslant 1.25$ nm. This trend is consistent with the dominance of one-photon-assisted electron tunneling as also evidenced by the log-log plot of $\mathcal{N}(E_0)$ calculated with TDDFT (not shown).

For large gap sizes $d_{\rm gap} \gtrsim 2$ nm, tunneling is negligible. As follows from the results shown in Fig. 12(a), optically induced electron transport is dominated by over-the-barrier transitions via multiphoton absorption. The effective photon order $n = 2$ is determined by the photoemission threshold. The calculated net electron transport is thus described by the $\mathcal{N}(d_{\rm gap}) \propto E_{\rm gap}^4$ dependence. Since $E_{\rm gap} = \mathcal{R}E_0$, for a fixed E_0 we obtain that $\mathcal{N}(d_{\rm gap})$ follows the variation of the local field enhancement in the gap $\mathcal{N}(d_{\rm gap}) \propto [\mathcal{R}(d_{\rm gap})]^4$ [see red dashed line in Fig. 12(c)]. Interestingly, the TDDFT results reproduce the variation of $\mathcal{N}$ by an order of magnitude measured experimentally by Lin and collaborators [41] as the gap size increases from about 1.5 nm to 4 nm (highlighted by the gray rectangle).

All in all, we have found that the TDDFT calculations performed in our model system are capable of reproducing the major trends observed experimentally for optically induced electron transport. These include the data obtained with 7-fs laser pulses used to drive electron transfer in the gap of a gold bowtie antenna [5], and the data obtained with cw illumination of a silver-based STM junction [41]. Importantly, our theoretical TDDFT approach is parameter free. The size of the junction (the key geometric parameter) has been set equal to that reported in the experiments. Our TDDFT study describes the "fast" [42] coherent component of the optically induced transport. It corresponds to the one-step process driven by the field of an optical pulse and it cannot be separated in time into excitation and tunneling (or over-the-barrier transfer) events. This said, electron relaxation leading, e.g., to thermionic emission [42], cannot be captured within the ALDA-TDDFT scheme [109–111]. Further theoretical work that explicitly incorporates excitation and relaxation events [43–48,106–108], as well as experimental investigations, are then needed in order to provide a more accurate picture of the process.

One remark is in order regarding possible effects of the band structure of the substrate. While d-electrons in noble

metals have binding energies several eV below the Fermi level, so that electron transport is dominated by the valence electrons, the projected band structure of the surface may affect electron transport by changing the surface reflectivity. Indeed, the Ag(111) surface used in Ref. [41] and the Cu(100) surface used in Refs. [40,41] are known to possess a projected band gap in the direction perpendicular to the surface. This gap extends to low binding energies in the case of Ag(111), or even above the vacuum level for Cu(100) [98]. The high reflectivity of the surface for electrons with energies inside the gap is behind the observation of field-emission resonances in STM [116–119]. While for Ag(111), at high applied bias, the transferred electron energies are above the band gap, this is not the case for $U < 1.6$ eV. A treatment of band structure effects is beyond the scope of this work and is noted for future investigation.

V. SUMMARY AND CONCLUSIONS AND OUTLOOK

In conclusion, we have theoretically investigated optically induced electron transport in metallic gaps ranging from sub-nanometer to several nanometers, with a particular focus on photon-assisted electron tunneling. Our work is relevant to STM junctions, optical nanoantennas, and other tunneling devices, as demonstrated by the comparison between our theoretical results and recent experimental observations.

As a representative system, we considered a junction formed by a dimer of parallel free-electron metal nanowires exposed to few-cycle and several-cycle laser pulses. The electron dynamics following optical excitation has been described using many-body time-dependent density-functional theory (TDDFT). Along with TDDFT, we also applied model approaches based on direct numerical and semiclassical strong-field theory solutions of the one-dimensional, one-electron time-dependent Schrödinger equation. These model approaches, and in particular the analytical semiclassical theory, are found to be extremely useful in providing guidelines for understanding the main trends calculated with TDDFT.

The conditions for photon-assisted electron tunneling are achieved by considering a sub-nm gap (here 0.8 nm), or considering a situation where an external dc bias is applied across wider (1-nm and 2-nm) gaps. The dc bias lowers the potential barrier between metals and enables optically assisted electron tunneling, as exploited in recent experiments.

In line with earlier findings, we confirm that an optical wave drives electron transport even in a more direct manner than merely producing electron excitation. The very electron ejection from the metal is locked to the waveform of the optical field. Electrons are launched at the metal-vacuum interface during the half-cycles of the optical field with the corresponding polarity.

While for single-cycle optical pulses this opens a possibility of CEP control of the net electron transfer $\mathcal{N}$, this control is only effective in the multiphoton regime, where the photon absorption orders ℓ driving electron transport satisfy $\ell \geqslant 2$. As we have demonstrated, in the single-photon regime of photon-assisted tunneling ($\ell = 1$), the CEP sensitivity of $\mathcal{N}$ vanishes. As a consequence, in a symmetric gap, the one-photon channel does not contribute to the net electron transfer across the gap, and $\ell = 2$ is the lowest photon order observed in the $\mathcal{N}(E_g)$ dependence at low fields in the gap E_g. In this situation, applying a dc bias breaks the symmetry of the system and allows the $\ell = 1$ channel of the photon-assisted tunneling to be observed provided the tunneling barrier is sufficiently low. In turn, this barrier can be controlled by an applied bias U and the gap size d_{gap}.

We have demonstrated that at low optical-field strengths in the gap, in the perturbative regime, the optically induced net electron transfer scales as $\mathcal{N} \propto E_g^{2\ell_{min}}$. This dependence reflects the lowest symmetry-allowed channel of photon-assisted tunneling (i.e., the lowest photon order). This lowest photon order is $\ell_{min} = 1$ for an asymmetric gap and $\ell_{min} = 2$ for a symmetric gap.

With increasing E_g, the perturbative regime of optically induced electron transport evolves into the multiphoton regime with a $\mathcal{N} \propto E_g^{2n}$ dependence of the net electron transfer on the optical-field strength. The *effective* photon order n reflects an average value over all active transport channels (tunneling and over-the-barrier) with $\ell \gtrsim \ell_{min}$ photon absorption. It follows from the TDDFT calculations that the transition between the perturbative and multiphoton regimes is relatively prompt, with n converging to the threshold of photoemission above the tunneling barrier $n \approx \mathcal{W}_{tb}/\omega$. This finding is in accord with semiclassical theory.

Using several-cycle optical pulses, representative of the experimental conditions, we qualitatively (and in some cases semiquantitatively) reproduce recent experimental data that dissect different photon channels in optically assisted tunneling. Because of the relatively long pulse duration, the CEP dependence is suppressed in this case. The contribution of different ℓ-photon channels of electron transport is controlled by the applied bias U and the gap size d_{gap}, which we set according to experiment. No fitting parameters are used, which strengthens the validity of approach and the mechanisms it uncovers. Furthermore, our results confirm that because of the localization of electron transfer within the junction region, the nanowire dimer model system is suitable for addressing photon-assisted tunneling in narrow gaps. This said, TDDFT captures the "fast" component of the photoemission, while quantifying the role of the relaxation of photoexcited electrons, as well as the "slow" thermionic part of electron emission [42], requires further theoretical work.

As possible future developments, we also foresee studying the role of the band structure of the substrate and addressing electron tunneling induced by short optical pulses with controlled frequency chirp.

We believe that the results presented in this work contribute to a deeper understanding and to the discussion of the physical mechanisms at play in electron transport induced in metallic junctions by optical pulses of single-cycle and longer duration. The processes and their control strategies, as studied here, are relevant for petahertz optoelectronic devices, as well as for scanning probe techniques targeting ultimate spatial and temporal resolution.

ACKNOWLEDGMENTS

A.G.B. gratefully acknowledges the warm hospitality of DIPC. B.M. and M.K. acknowledge funding from the Euro-

pean Union's Horizon 2020 research and innovation program under Grant Agreement No. 853393-ERC-ATTIDA and from the Israel Science Foundation (ISF) under Grant No. 1504/20, as well as partial financial support from the Helen Diller Quantum Center at the Technion. J.A. and A.B. acknowledge financial support from Grant No. IT 1526-22 funded by the Department of Science, Universities and Innovation of the Basque Government.

DATA AVAILABILITY

The data that support the findings of this article are not publicly available upon publication because it is not technically feasible and/or the cost of preparing, depositing, and hosting the data would be prohibitive within the terms of this research project. The data are available from the authors upon reasonable request.

APPENDIX A: TDDFT CALCULATIONS WITH AN APPLIED DC BIAS

As we discussed in Sec. II A, in order to study the role of an applied dc bias the dimer is subjected to slowly varying THz field. The corresponding potential, introduced into the time-dependent KS equations of the TDDFT, is given by

$$V_{\mathrm{THz}}(x,t) = -x\,\frac{\tilde{U}}{d_{\mathrm{gap}}}\,\mathcal{U}(t-t_-). \tag{A1}$$

The switching function $\mathcal{U}$ is defined as

$$\mathcal{U}(\xi) = \begin{cases} 0, & \xi < -\tau_{\mathrm{THz}}, \\ \sin^2\left(\frac{\pi}{2}\,\frac{\xi+\tau_{\mathrm{THz}}}{\tau_{\mathrm{THz}}}\right), & -\tau_{\mathrm{THz}} \leqslant \xi \leqslant 0, \\ 1, & 0 < \xi. \end{cases} \tag{A2}$$

Typically, we choose a switching time $\tau_{\mathrm{THz}} = 50$ fs and $t_- = -3.5\tau$ so that at the moment of the arrival of the optical pulse the system is polarized by a nearly constant electric field $\tilde{U}/d_{\mathrm{gap}}$. The effective dc bias U is given by the difference between the self-consistent potentials inside the left and the right cylinders at $t = t_-$:

$$U = V(-R - d_{\mathrm{gap}}/2, 0, t) - V(R + d_{\mathrm{gap}}/2, 0, t), \tag{A3}$$

and it equals to the difference between the Fermi energies of the cylinders. Note that $U \neq \tilde{U}$ because of the cylindrical geometry and small charge transfer during the rise of the THz field.

APPENDIX B: PHOTOEMISSION FORMULAS

With Eqs. (15) and (17), we give expressions for electron transfer probability $\mathcal{P}_{L\to R}$ and the action function $S(t_{2\mathrm{s}}, t_{1\mathrm{s}})$, respectively. For convenience we repeat the definition of the latter here:

$$S(t_{2\mathrm{s}}, t_{1\mathrm{s}}) = \mathcal{E}t_{2\mathrm{s}} + \frac{\tilde{p}^2}{2}(t_{2\mathrm{s}} - t_{1\mathrm{s}}) - \int_{t_{1\mathrm{s}}}^{t_{2\mathrm{s}}} \frac{A_{\mathrm{opt}}^2(t')}{2}\,dt' - \int_{t_{1\mathrm{s}}}^{t_{2\mathrm{s}}} V_{\mathrm{m}}[x(t')]\,dt' - \mathcal{E}_F t_{1\mathrm{s}}, \tag{B1}$$

and the corresponding electron transfer probability from the left to the right is expressed as

$$\mathcal{P}_{L\to R} \propto \sum_{\mathcal{E}} e^{-2\mathrm{Im}[S(t_{2\mathrm{s}}, t_{1\mathrm{s}})]}. \tag{B2}$$

For a strong optical field where $\zeta < 1$, we have

$$\mathrm{Im}[t_{1\mathrm{s}}] \equiv \mathrm{Im}[t_{\mathrm{L}}] = \frac{E_{\mathrm{g}}\sqrt{1+\gamma^2}}{E_{\mathrm{bias}} + E_{\mathrm{g}}\sqrt{1+\gamma^2}}\,\frac{\ln(\gamma + \sqrt{1+\gamma^2})}{\omega} \tag{B3}$$

and

$$\mathrm{Im}\big[t_{2\mathrm{s}}\big] = 0,\ \mathrm{Im}[\tilde{p}] \approx 0. \tag{B4}$$

Substituting these solutions into Eq. (B1), we obtain

$$\mathrm{Im}\big[\mathcal{E}t_{2\mathrm{s}}\big] = \mathrm{Im}\left[\frac{\tilde{p}^2}{2}(t_{2\mathrm{s}} - t_{1\mathrm{s}})\right] = 0, \tag{B5}$$

as well as

$$\mathrm{Im}\left[\int_{t_{1\mathrm{s}}}^{t_{2\mathrm{s}}} \frac{A^2(t')}{2}\,dt'\right] = \frac{\overline{\mathcal{W}}_{\mathrm{tb}}}{2\omega\gamma^2}\left\{\sinh\left[\omega\mathrm{Im}\big(t_{1\mathrm{s}}\big)\right]\cosh\left[\omega\mathrm{Im}\big(t_{1\mathrm{s}}\big)\right] - \omega\mathrm{Im}\big(t_{1\mathrm{s}}\big)\right\} - \frac{E_{\mathrm{g}}E_{\mathrm{bias}}}{\omega^3}\left\{\sinh\left[\omega\mathrm{Im}\big(t_{1\mathrm{s}}\big)\right] - \omega\mathrm{Im}(t_{1\mathrm{s}})\cosh\left[\omega\mathrm{Im}\big(t_{1\mathrm{s}}\big)\right]\right\}, \tag{B6}$$

and

$$\mathrm{Im}\left[\int_{t_{1\mathrm{s}}}^{t_{2\mathrm{s}}} V_{\mathrm{m}}[x(t')]\,dt'\right] = -\overline{V}_{\mathrm{m}}\,\mathrm{Im}[t_{1\mathrm{s}}]. \tag{B7}$$

Depending on the value of the Keldysh parameter γ we distinguish two situations:

Case: $\gamma \gg 1$. In the multiphoton regime where $\gamma \gg 1$, substituting the above solutions into the Eq. (B2) and replacing the emission time with

$$\mathrm{Im}[t_{1\mathrm{s}}] = \frac{\omega\sqrt{\overline{\mathcal{W}}_{\mathrm{tb}}}}{E_{\mathrm{bias}} + \omega\sqrt{\overline{\mathcal{W}}_{\mathrm{tb}}}}\,\frac{\ln(2\gamma)}{\omega}, \tag{B8}$$

we obtain the formula describing the multiphoton regime:

$$\mathcal{P}_{L\to R} \propto (2\gamma)^{-2\left(\Upsilon\frac{\overline{\mathcal{W}}_{\mathrm{tb}}}{\omega}\right)} \times (2\gamma)^{\frac{2\Upsilon E_{\mathrm{bias}}E_{\mathrm{g}}}{\omega^3}\cosh[\Upsilon\ln(2\gamma)]}\cdots, \tag{B9}$$

where

$$\Upsilon \equiv \frac{\omega\sqrt{2\overline{\mathcal{W}}_{\mathrm{tb}}}}{E_{\mathrm{bias}} + \omega\sqrt{2\overline{\mathcal{W}}_{\mathrm{tb}}}}. \tag{B10}$$

Case: $\gamma \ll 1$. In the tunneling regime, $\gamma \ll 1$. As a result, we obtain

$$\mathrm{Im}[t_{1\mathrm{s}}] = \frac{\sqrt{2\overline{\mathcal{W}}_{\mathrm{tb}}}}{E_{\mathrm{bias}} + E_{\mathrm{g}}}. \tag{B11}$$

Substituting this approximation into Eq. (B2), we obtain the formula for the probability of the field-driven tunneling:

$$\mathcal{P}_{L\to R} \propto \exp\left[-\frac{2(2\overline{\mathcal{W}}_{\mathrm{tb}})^{\frac{3}{2}}}{3(E_{\mathrm{bias}} + E_{\mathrm{g}})}\right]. \tag{B12}$$

APPENDIX C: TRANSPORT ASSISTED BY ONE-PHOTON ABSORPTION, PERTURBATIVE TREATMENT FOR THE SMALL OPTICAL FIELD

Let us assume for simplicity that the electronic coupling between the nanowires and thus tunneling can be neglected in the ground-state system. This implies that $\langle\psi_k^p|\psi_{k'}^{p'}\rangle = \delta_{k,k'}\delta_{p,p'}$ where k and k' label the ground-state bound KS orbitals localized in the left (L) and right (R) nanowires as indicated with $(p, p') = (L, R)$ (see Fig. 2 for geometry). Here, δ is the Kronecker delta. For identical cylindrical nanowires the energies $\mathcal{E}_k$ of the K-S orbitals are given by $\hat{H}_0\psi_k^p = \mathcal{E}_k\psi_k^p$ where $\hat{H}_0$ is the ground state Hamiltonian. For an initial state given by the KS orbital localized in the left nanowire $\psi_k^L(\mathbf{r})$, the time-dependent wave function $\Psi_k^L(\mathbf{r}, t)$ is obtained within the TDDFT from the solution of the time-dependent K-S equation

$$i\partial_t\Psi_k^L(\mathbf{r}, t) = \{\hat{H}_0 + \delta V(\mathbf{r}, t)\}\Psi_k^L(\mathbf{r}, t), \tag{C1}$$

where $\delta V(\mathbf{r}, t) = V_{\rm opt}(\mathbf{r}, t) + V_{\rm ind}(\mathbf{r}, t)$ is the (small) time-dependent potential. It is given by the sum of the potential $V_{\rm opt}(x, t) = x\ a(t)\cos(\omega t + \varphi)$ owing to the incident field [$a(t)$ is the slow envelope function] and the self-consistent response of the system $V_{\rm ind}(\mathbf{r}, t) = V(\mathbf{r}, t) - V_{\rm gs}(\mathbf{r})$. The latter accounts for the difference between the self-consistent time-dependent and ground-state potentials. For the sake of brevity, below we drop off the coordinate variables. We are interested in the weak-field regime. Therefore, we use perturbation theory and linear response to describe the one-photon absorption process. With the wave function sought in the form $\Psi_k^L(t) = e^{-i\mathcal{E}_k t}\psi_k^L + \delta\Psi_k^L(t)$, where $\delta\Psi_k^L(t)$ is the perturbation, and keeping only the first-order terms in δV we obtain

$$\{i\partial_t - \hat{H}_0\}\delta\Psi_k^L(t) = \delta V(t)e^{-i\mathcal{E}_k t}\psi_k^L. \tag{C2}$$

The potential δV can be found from

$$\delta V(t) = \int_0^\infty d\omega'\ e^{-i\omega' t}\ [1 + \hat{\alpha}(\omega')]\ V_{\rm opt}(\omega') + \text{c.c.}, \tag{C3}$$

where $\hat{\alpha}(\omega, \mathbf{r}, \mathbf{r}')$ is the response tensor, c.c. stands for the complex conjugate, and $V_{\rm opt}(\omega')$ is obtained from

$$\begin{aligned} V_{\rm opt}(\omega') &= \frac{1}{2\pi}\int_{-\infty}^{\infty} dt e^{i\omega' t}V_{\rm opt}(t) \\ &= \frac{x}{2}[e^{i\varphi}a(\omega' + \omega) + e^{-i\varphi}a(\omega' - \omega)]. \end{aligned} \tag{C4}$$

Since $a(t)$ is a slowly varying function only the second term of Eq. (C4) will contribute to $\delta V(t)$ given by Eq. (C3). Applying the rotating-wave approximation we arrive at

$$\{i\partial t - \hat{H}_0\}\delta\Psi_k^L(t) = e^{-i\varphi}e^{-i\mathcal{E}_k t}\delta v(t)\psi_k^L, \tag{C5}$$

where

$$\delta v(t) = \frac{1}{2}\int_0^\infty d\omega' e^{-i\omega' t}[1 + \hat{\alpha}(\omega')]\ x\ a(\omega' - \omega). \tag{C6}$$

Finally, from Eq. (C5) $\delta\Psi_k^L(t)$ can be found from

$$\delta\Psi_k^L(t) = \frac{e^{-i\varphi}}{i}\int_{-\infty}^{t} dt' e^{-i\hat{H}_0(t-t')}e^{-i\mathcal{E}_k t'}\delta v(t')\psi_k^L. \tag{C7}$$

The electron transfer probability to the right nanowire is given by

$$\mathcal{P}_{(L,k)\to R}(\varphi) = \sum_\nu \left|\langle\psi_\nu^R|\delta\Psi_k^L(t\to\infty)\rangle\right|^2. \tag{C8}$$

From Eqs. (C7) and (C8), it follows that $\mathcal{P}_{(L,k)\to R}$ is independent of CEP given by φ. Consider now an initial state given by the ground-state KS orbital localized in the right nanowire. From the symmetry of the system $\mathcal{P}_{(R,k)\to L}(\varphi) = \mathcal{P}_{(L,k)\to R}(\varphi + \pi)$, and from the demonstration above it follows then that $\mathcal{P}_{(R,k)\to L}(\varphi) = \mathcal{P}_{(L,k)\to R}(\varphi)$. The net electron transfer $\mathcal{N} = \sum_k \chi_k\{\mathcal{P}_{(L,k)\to R}(\varphi) - \mathcal{P}_{(R,k)\to L}(\varphi)\} = 0$. Here, the summation runs over occupied KS orbitals and χ_k accounts for the spin statistical factors and degeneracy associated with z motion. We therefore conclude that if only one-photon absorption is considered, then $\mathcal{N}$ is zero for a symmetric system.

[1] S. Yoshida, H. Hirori, T. Tachizaki, K. Yoshioka, Y. Arashida, Z.-H. Wang, Y. Sanari, O. Takeuchi, Y. Kanemitsu, and H. Shigekawa, Subcycle transient scanning tunneling spectroscopy with visualization of enhanced terahertz near field, ACS Photonics **6**, 1356 (2019).

[2] Y. Arashida, H. Mogi, M. Ishikawa, I. Igarashi, A. Hatanaka, N. Umeda, J. Peng, S. Yoshida, O. Takeuchi, and H. Shigekawa, Subcycle mid-infrared electric-field-driven scanning tunneling microscopy with a time resolution higher than 30 fs, ACS Photonics **9**, 3156 (2022).

[3] S. Liu, A. Hammud, I. Hamada, M. Wolf, M. Müller, and T. Kumagai, Nanoscale coherent phonon spectroscopy, Sci. Adv. **8**, eabq5682 (2022).

[4] M. Garg, A. Martin-Jimenez, M. Pisarra, Y. Luo, F. Martín, and K. Kern, Visualizing hot carrier dynamics by nonlinear optical spectroscopy at the atomic length scale, Nat. Photonics **16**, 196 (2022).

[5] Y. Luo, F. Neubrech, A. Martin-Jimenez, N. Liu, K. Kern, and M. Garg, Real-time tracking of coherent oscillations of electrons in a nanodevice by photo-assisted tunnelling, Nat. Commun. **15**, 1316 (2024).

[6] Y. Luo, S. Sheng, A. Schirato, A. Martin-Jimenez, G. Della Valle, G. Cerullo, K. Kern, and M. Garg, Visualizing hot carrier dynamics by nonlinear optical spectroscopy at the atomic length scale, Nat. Commun. **16**, 4999 (2025).

[7] S. Maier, R. Spachtholz, K. Glöckl, C. M. Bustamante, S. Lingl, M. Maczejka, J. Schön, F. J. Giessibl, F. P. Bonafé, M. A. Huber, A. Rubio, J. Repp, and R. Huber, Attosecond charge transfer in atomic-resolution scanning tunneling microscopy, arXiv:2507.10206.

[8] P. Dombi, Z. Pápa, J. Vogelsang, S. V. Yalunin, M. Sivis, G. Herink, S. Schäfer, P. Groß, C. Ropers, and C. Lienau, Strong-field nano-optics, Rev. Mod. Phys. **92**, 025003 (2020).

[9] M. Müller, Imaging surfaces at the space-time limit: New perspectives of time-resolved scanning tunneling microscopy for ultrafast surface science, Prog. Surf. Sci. **99**, 100727 (2024).

[10] J. Vogelsang, A. Mikkelsen, C. Ropers, J. H. Gaida, M. Garg, K. Kern, J. Miao, M. Schultze, and M. Ossiander,

Attosecond microscopy - advances and outlook, Europhys. Lett. **149**, 36001 (2025).

[11] Z. Zhao, V. Kravtsov, Z. Wang, Z. Zhou, L. Dou, D. Huang, Z. Wang, X. Cheng, M. B. Raschke, and T. Jiang, Applications of ultrafast nano-spectroscopy and nano-imaging with tip-based microscopy, eLight **5**, 1 (2025).

[12] T. L. Cocker, V. Jelic, M. Gupta, S. J. Molesky, J. A. J. Burgess, G. De Los Reyes, L. V. Titova, Y. Y. Tsui, M. R. Freeman, and F. A. Hegmann, An ultrafast terahertz scanning tunneling microscope, Nat. Photonics **7**, 620 (2013).

[13] K. Yoshioka, I. Katayama, Y. Minami, M. Kitajima, S. Yoshida, H. Shigekawa, and J. Takeda, Real-space coherent manipulation of electrons in a single tunnel junction by single-cycle terahertz electric fields, Nat. Photonics **10**, 762 (2016).

[14] T. L. Cocker, D. Peller, P. Yu, J. Repp, and R. Huber, Tracking the ultrafast motion of a single molecule by femtosecond orbital imaging, Nature (London) **539**, 263 (2016).

[15] C. Roelcke, L. Z. Kastner, M. Graml, A. Biereder, J. Wilhelm, J. Repp, R. Huber, and Y. A. Gerasimenko, Ultrafast atomic-scale scanning tunneling spectroscopy of a single vacancy in a monolayer crystal, Nat. Photonics **18**, 595 (2024).

[16] V. Jelic, S. Adams, M. Hassan, K. Cleland-Host, S. E. Ammerman, and T. L. Cocker, Atomic-scale terahertz time-domain spectroscopy, Nat. Photonics **18**, 898 (2024).

[17] S. Sheng, S. Abdo, S. Rolf-Pissarczyk, K. Lichtenberg, S. Baumann, J. A. J. Burgess, L. Malavolti, and S. Loth, Terahertz spectroscopy of collective charge density wave dynamics at the atomic scale, Nat. Phys. **20**, 1603 (2024).

[18] W. Schattke and M. A. Van Hove, *Solid-state Photoemission and Related Methods: Theory and Experiment* (Wiley, Hoboken, NJ, 2003).

[19] M. Daąbrowski, Y. Dai, and H. Petek, Ultrafast photoemission electron microscopy: Imaging plasmons in space and time, Chem. Rev. **120**, 6247 (2020).

[20] M. Bauer, A. Marienfeld, and M. Aeschlimann, Hot electron lifetimes in metals probed by time-resolved two-photon photoemission, Prog. Surf. Sci. **90**, 319 (2015).

[21] C. Lemell, X.-M. Tong, F. Krausz, and J. Burgdörfer, Electron emission from metal surfaces by ultrashort pulses: Determination of the carrier-envelope phase, Phys. Rev. Lett. **90**, 076403 (2003).

[22] C. Ropers, D. R. Solli, C. P. Schulz, C. Lienau, and T. Elsaesser, Localized multiphoton emission of femtosecond electron pulses from metal nanotips, Phys. Rev. Lett. **98**, 043907 (2007).

[23] R. Bormann, M. Gulde, A. Weismann, S. V. Yalunin, and C. Ropers, Tip-enhanced strong-field photoemission, Phys. Rev. Lett. **105**, 147601 (2010).

[24] M. Krüger, M. Schenk, P. Hommelhoff, G. Wachter, C. Lemell, and J. Burgdörfer, Interaction of ultrashort laser pulses with metal nanotips: A model system for strong-field phenomena, New J. Phys. **14**, 085019 (2012).

[25] D. J. Park, B. Piglosiewicz, S. Schmidt, H. Kollmann, M. Mascheck, and C. Lienau, Strong field acceleration and steering of ultrafast electron pulses from a sharp metallic nanotip, Phys. Rev. Lett. **109**, 244803 (2012).

[26] P. Dombi, A. Hörl, P. Rácz, I. Márton, A. Trügler, J. R. Krenn, and U. Hohenester, Ultrafast strong-field photoemission from plasmonic nanoparticles, Nano Lett. **13**, 674 (2013).

[27] J. Passig, S. Zherebtsov, R. Irsig, M. Arbeiter, C. Peltz, S. Göde, S. Skruszewicz, K.-H. Meiwes-Broer, J. Tiggesbäumker, M. F. Kling, and T. Fennel, Nanoplasmonic electron acceleration by attosecond-controlled forward rescattering in silver clusters, Nat. Commun. **8**, 1181 (2017).

[28] M. Krüger, C. Lemell, G. Wachter, J. Burgdörfer, and P. Hommelhoff, Attosecond physics phenomena at nanometric tips, J. Phys. B: At. Mol. Opt. Phys. **51**, 172001 (2018).

[29] P. D. Keathley, W. P. Putnam, P. Vasireddy, R. G. Hobbs, Y. Yang, K. K. Berggren, and F. X. Kärtner, Vanishing carrier-envelope-phase-sensitive response in optical-field photoemission from plasmonic nanoantennas, Nat. Phys. **15**, 1128 (2019).

[30] M. F. Ciappina, J. A. Pérez-Hernández, A. S. Landsman, W. A. Okell, S. Zherebtsov, B. Förg, J. Schötz, L. Seiffert, T. Fennel, T. Shaaran, T. Zimmermann, A. Chacón, R. Guichard, A. Zaïr, J. W. G. Tisch, J. P. Marangos, T. Witting, A. Braun, S. A. Maier, L. Roso, *et al.*, Attosecond physics at the nanoscale, Rep. Prog. Phys. **80**, 054401 (2017).

[31] P. Dienstbier, L. Seiffert, T. Paschen, A. Liehl, A. Leitenstorfer, T. Fennel, and P. Hommelhoff, Tracing attosecond electron emission from a nanometric metal tip, Nature (London) **616**, 702 (2023).

[32] C. Heide, P. D. Keathley, and M. F. Kling, Petahertz electronics, Nat. Rev. Phys. **6**, 648 (2024).

[33] M. Büttiker and R. Landauer, Traversal time for tunneling, Phys. Rev. Lett. **49**, 1739 (1982).

[34] M. H. Pedersen and M. Büttiker, Scattering theory of photon-assisted electron transport, Phys. Rev. B **58**, 12993 (1998).

[35] P. K. Tien and J. P. Gordon, Multiphoton process observed in the interaction of microwave fields with the tunneling between superconductor films, Phys. Rev. **129**, 647 (1963).

[36] J. R. Tucker and M. J. Feldman, Quantum detection at millimeter wavelengths, Rev. Mod. Phys. **57**, 1055 (1985).

[37] G. Platero and R. Aguado, Photon-assisted transport in semiconductor nanostructures, Phys. Rep. **395**, 1 (2004).

[38] S. Kohler, J. Lehmann, and P. Hänggi, Driven quantum transport on the nanoscale, Phys. Rep. **406**, 379 (2005).

[39] H. Yanagisawa, C. Hafner, P. Doná, M. Klöckner, D. Leuenberger, T. Greber, M. Hengsberger, and J. Osterwalder, Optical control of field-emission sites by femtosecond laser pulses, Phys. Rev. Lett. **103**, 257603 (2009).

[40] B. Schröder, O. Bunjes, L. Wimmer, K. Kaiser, G. A. Traeger, T. Kotzott, C. Ropers, and M. Wenderoth, Controlling photocurrent channels in scanning tunneling microscopy, New J. Phys. **22**, 033047 (2020).

[41] C. Lin, F. Krecinic, H. Yoshino, A. Hammud, A. Pan, M. Wolf, M. Müller, and T. Kumagai, Continuous-wave multiphoton-induced electron transfer in tunnel junctions driven by intense plasmonic fields, ACS Photonics **10**, 3637 (2023).

[42] N. Martín Sabanés, F. Krecinic, T. Kumagai, F. Schulz, M. Wolf, and M. Müller, Femtosecond thermal and nonthermal hot electron tunneling inside a photoexcited tunnel junction, ACS Nano **16**, 14479 (2022).

[43] G. Tagliabue, A. S. Jermyn, R. Sundararaman, A. J. Welch, J. S. DuChene, R. Pala, A. R. Davoyan, P. Narang, and H. A. Atwater, Quantifying the role of surface plasmon excitation and hot carrier transport in plasmonic devices, Nat. Commun. **9**, 3394 (2018).

[44] Y. Dubi and Y. Sivan, Hot electrons in metallic nanostructures-non-thermal carriers or heating? Light: Sci. Appl. **8**, 89 (2019).
[45] A. Schirato, M. Maiuri, G. Cerullo, and G. D. Valle, Ultrafast hot electron dynamics in plasmonic nanostructures: Experiments, modeling, design, Nanophotonics **12**, 1 (2023).
[46] J. Khurgin, A. Y. Bykov, and A. V. Zayats, Hot-electron dynamics in plasmonic nanostructures: Fundamentals, applications and overlooked aspects, eLight **4**, 15 (2024).
[47] F. Kiani, A. R. Bowman, M. Sabzehparvar, R. Sundararaman, and G. Tagliabue, Distinguishing inner and outer-sphere hot electron transfer in Au/p-GaN photocathodes, Nano Lett. **24**, 16008 (2024).
[48] A. Stefancu, N. J. Halas, P. Nordlander, and E. Cortes, Electronic excitations at the plasmon-molecule interface, Nat. Phys. **20**, 1065 (2024).
[49] M. Garg and K. Kern, Attosecond coherent manipulation of electrons in tunneling microscopy, Science **367**, 411 (2020).
[50] D. Davidovich, B. Ma, A. Goldner, S. Cohen, Z. Chen, and M. Krüger, Clocking and controlling attosecond currents in a scanning tunneling microscope, arXiv:2507.10252.
[51] M. Förster, T. Paschen, M. Krüger, C. Lemell, G. Wachter, F. Libisch, T. Madlener, J. Burgdörfer, and P. Hommelhoff, Two-color coherent control of femtosecond above-threshold photoemission from a tungsten nanotip, Phys. Rev. Lett. **117**, 217601 (2016).
[52] T. Paschen, M. Förster, M. Krüger, C. Lemell, G. Wachter, F. Libisch, T. Madlener, J. Burgdörfer, and P. Hommelhoff, High visibility in two-color above-threshold photoemission from tungsten nanotips in a coherent control scheme, J. Mod. Opt. **64**, 1054 (2017).
[53] P. Dienstbier, T. Paschen, and P. Hommelhoff, Coherent control at gold needle tips approaching the strong-field regime, Nanophotonics **10**, 3717 (2021).
[54] A. Li, Y. Pan, P. Dienstbier, and P. Hommelhoff, Quantum interference visibility spectroscopy in two-color photoemission from tungsten needle tips, Phys. Rev. Lett. **126**, 137403 (2021).
[55] H. Y. Kim, M. Garg, S. Mandal, L. Seiffert, T. Fennel, and E. Goulielmakis, Attosecond field emission, Nature (London) **613**, 662 (2023).
[56] S. V. Yalunin, M. Gulde, and C. Ropers, Strong-field photoemission from surfaces: Theoretical approaches, Phys. Rev. B **84**, 195426 (2011).
[57] G. Wachter, C. Lemell, J. Burgdörfer, M. Schenk, M. Krüger, and P. Hommelhoff, Electron rescattering at metal nanotips induced by ultrashort laser pulses, Phys. Rev. B **86**, 035402 (2012).
[58] L. Shi, I. Babushkin, A. Husakou, O. Melchert, B. Frank, J. Yi, G. Wetzel, A. Demircan, C. Lienau, H. Giessen, M. Ivanov, U. Morgner, and M. Kovacev, Femtosecond field-driven on-chip unidirectional electronic currents in nonadiabatic tunneling regime, Laser Photon. Rev. **15**, 2000475 (2021).
[59] S. Kim, T. Schmude, G. Burkard, and A. S. Moskalenko, Quasiclassical theory of non-adiabatic tunneling in nanocontacts induced by phase-controlled ultrashort light pulses, New J. Phys. **23**, 083006 (2021).
[60] Y. Luo and P. Zhang, Optical-field-induced electron emission in a dc-biased nanogap, Phys. Rev. Appl. **17**, 044008 (2022).
[61] F. Ritzkowsky, M. Yeung, E. Bebeti, T. Gebert, T. Matsuyama, M. Budden, R. E. Mainz, H. Cankaya, K. K. Berggren, G. M. Rossi, P. D. Keathley, and F. X. Kärtner, On-chip petahertz electronics for single-shot phase detection, Nat. Commun. **15**, 10179 (2024).
[62] M. Ludwig, A. K. Kazansky, G. Aguirregabiria, D. C. Marinica, M. Falk, A. Leitenstorfer, D. Brida, J. Aizpurua, and A. G. Borisov, Active control of ultrafast electron dynamics in plasmonic gaps using an applied bias, Phys. Rev. B **101**, 241412(R) (2020).
[63] A. G. Borisov, B. Ma, M. Zapata-Herrera, A. Babaze, M. Krüger, and J. Aizpurua, Femtosecond optical-field-driven currents in few-nanometer-size gaps with hot electron injection into metallic leads, ACS Photonics **12**, 2137 (2025).
[64] B. Ma and M. Krüger, Robust strong-field theory model for ultrafast electron transport through metal-insulator-metal tunneling nanojunctions, Phys. Rev. A **112**, 033104 (2025).
[65] H. R. Reiss, Foundations of the strong-field approximation, in *Progress in Ultrafast Intense Laser Science III* (Springer, Berlin, 2008), pp. 1–31.
[66] D. B. Milošević, G. G. Paulus, D. Bauer, and W. Becker, Above-threshold ionization by few-cycle pulses, J. Phys. B: At., Mol. Opt. Phys. **39**, R203(R) (2006).
[67] B. Ma and M. Krüger, Strong-field theory of attosecond tunneling microscopy, Phys. Rev. Lett. **133**, 236901 (2024).
[68] M. Turchetti, M. R. Bionta, Y. Yang, F. Ritzkowsky, D. R. Candido, M. E. Flatté, K. K. Berggren, and P. D. Keathley, Impact of dc bias on weak optical-field-driven electron emission in nano-vacuum-gap detectors, J. Opt. Soc. Am. B **38**, 1009 (2021).
[69] A. Thon, M. Merschdorf, W. Pfeiffer, T. Klamroth, P. Saalfrank, and D. Diesing, Photon-assisted tunneling versus tunneling of excited electrons in metal-insulator-metal junctions, Appl. Phys. A **78**, 189 (2004).
[70] M. Ludwig, G. Aguirregabiria, F. Ritzkowsky, T. Rybka, D. C. Marinica, J. Aizpurua, A. G. Borisov, A. Leitenstorfer, and D. Brida, Sub-femtosecond electron transport in a nanoscale gap, Nat. Phys. **16**, 341 (2020).
[71] Z. Hu, Y. Kwok, G. Chen, and S. Mukamel, Carrier-envelope-phase modulated currents in scanning tunneling microscopy, Nano Lett. **21**, 6569 (2021).
[72] L. Bhan, C. Covington, and K. Varga, Signatures of atomic structure in subfemtosecond laser-driven electron dynamics in nanogaps, Phys. Rev. B **105**, 085416 (2022).
[73] L. Chen, Y. Zhang, G. Chen, and I. Franco, Stark control of electrons along nanojunctions, Nat. Commun. **9**, 2070 (2018).
[74] D. Diesing, M. Merschdorf, A. Thon, and W. Pfeiffer, Identification of multiphoton induced photocurrents in metal-insulator-metal junctions, Appl. Phys. B **78**, 443 (2004).
[75] T. Siday, J. Hayes, F. Schiegl, F. Sandner, P. Menden, V. Bergbauer, M. Zizlsperger, S. Nerreter, S. Lingl, J. Repp, J. Wilhelm, M. A. Huber, Y. A. Gerasimenko, and R. Huber, All-optical subcycle microscopy on atomic length scales, Nature (London) **629**, 329 (2024).
[76] P. Dombi, A. Apolonski, C. Lemell, G. G. Paulus, M. Kakehata, R. Holzwarth, T. Udem, K. Torizuka, J. Burgdörfer, T. W. Hänsch, and F. Krausz, Direct measurement and analysis of the carrier-envelope phase in light pulses approaching the single-cycle regime, New J. Phys. **6**, 39 (2004).

[77] A. Apolonski, P. Dombi, G. G. Paulus, M. Kakehata, R. Holzwarth, T. Udem, C. Lemell, K. Torizuka, J. Burgdörfer, T. W. Hänsch, and F. Krausz, Observation of light-phase-sensitive photoemission from a metal, Phys. Rev. Lett. **92**, 073902 (2004).

[78] T. V. Teperik, P. Nordlander, J. Aizpurua, and A. G. Borisov, Quantum effects and nonlocality in strongly coupled plasmonic nanowire dimers, Opt. Express **21**, 27306 (2013).

[79] T. Rybka, M. Ludwig, M. F. Schmalz, V. Knittel, D. Brida, and A. Leitenstorfer, Sub-cycle optical phase control of nanotunnelling in the single-electron regime, Nat. Photonics **10**, 667 (2016).

[80] P. Rácz, Z. Pápa, I. Márton, J. Budai, P. Wróbel, T. Stefaniuk, C. Prietl, J. R. Krenn, and P. Dombi, Measurement of nanoplasmonic field enhancement with ultrafast photoemission, Nano Lett. **17**, 1181 (2017).

[81] J. P. Perdew, H. Q. Tran, and E. D. Smith, Stabilized jellium: Structureless pseudopotential model for the cohesive and surface properties of metals, Phys. Rev. B **42**, 11627 (1990).

[82] M. A. L. Marques and E. K. U. Gross, Time-dependent density functional theory, Annu. Rev. Phys. Chem. **55**, 427 (2004).

[83] O. Gunnarsson and B. Lundqvist, Exchange and correlation in atoms, molecules, and solids by the spin-density-functional formalism, Phys. Rev. B **13**, 4274 (1976).

[84] D. Kosloff and R. Kosloff, A Fourier method solution for the time dependent Schrödinger equation as a tool in molecular dynamics, J. Comput. Phys. **52**, 35 (1983).

[85] C. Leforestier, R. H. Bisseling, C. Cerjan, M. D. Feit, R. Friesner, A. Guldberg, A. Hammerich, C. Jolicard, W. Karrlein, H.-D. Meyer, N. Lipkin, O. Roncero, and R. Kosloff, A comparison of different propagation schemes for the time dependent Schrödinger equation, J. Comput. Phys. **94**, 59 (1991).

[86] R. M. Dreizler and E. K. U. Gross, The Kohn-Sham scheme, in *Density Functional Theory: An Approach to the Quantum Many-Body Problem* (Springer, Berlin, 1990), pp. 43–74.

[87] P. Hommelhoff, C. Kealhofer, and M. A. Kasevich, Ultrafast electron pulses from a tungsten tip triggered by low-power femtosecond laser pulses, Phys. Rev. Lett. **97**, 247402 (2006).

[88] M. Eldar, S. Abo-Toame, and M. Krüger, Sub-optical-cycle electron pulse trains from metal nanotips, J. Phys. B: At. Mol. Opt. Phys. **55**, 074001 (2022).

[89] M. Yeung, L.-T. Chou, M. Turchetti, F. Ritzkowsky, K. K. Berggren, and P. D. Keathley, Lightwave-electronic harmonic frequency mixing, Sci. Adv. **10**, eadq0642 (2024).

[90] J. Pitarke, F. Flores, and P. Echenique, Tunneling spectroscopy: Surface geometry and interface potential effects, Surf. Sci. **234**, 1 (1990).

[91] R. O. Jones, P. J. Jennings, and O. Jepsen, Surface barrier in metals: A new model with application to W(001), Phys. Rev. B **29**, 6474 (1984).

[92] A. G. Eguiluz, M. Heinrichsmeier, A. Fleszar, and W. Hanke, First-principles evaluation of the surface barrier for a Kohn-Sham electron at a metal surface, Phys. Rev. Lett. **68**, 1359 (1992).

[93] I. D. White, R. W. Godby, M. M. Rieger, and R. J. Needs, Dynamic image potential at an Al(111) surface, Phys. Rev. Lett. **80**, 4265 (1998).

[94] L. V. Keldysh, Ionization in the field of a strong electromagnetic wave, J. Exptl. Theoret. Phys. (U.S.S.R.) **47**, 1945 (1964) [Sov. Phys.–JETP **20**, 1307 (1965)].

[95] D. J. Park and Y. H. Ahn, Ultrashort field emission in metallic nanostructures and low-dimensional carbon materials, Adv. Phys.: X **5**, 1726207 (2020).

[96] F. Kusa, K. E. Echternkamp, G. Herink, C. Ropers, and S. Ashihara, Optical field emission from resonant gold nanorods driven by femtosecond mid-infrared pulses, AIP Adv. **5**, 077138 (2015).

[97] W. P. Putnam, R. G. Hobbs, P. D. Keathley, K. K. Berggren, and F. X. Kärtner, Optical-field-controlled photoemission from plasmonic nanoparticles, Nat. Phys. **13**, 335 (2017).

[98] E. V. Chulkov, V. M. Silkin, and P. M. Echenique, Image potential states on metal surfaces: Binding energies and wave functions, Surf. Sci. **437**, 330 (1999).

[99] J. Schoetz, Z. Wang, E. Pisanty, M. Lewenstein, M. F. Kling, and M. F. Ciappina, Perspective on petahertz electronics and attosecond nanoscopy, ACS Photonics **6**, 3057 (2019).

[100] A. Rossetti, F. Pagnini, M. Assaid, C. Schönfeld, A. Leitenstorfer, M. Ludwig, and D. Brida, Modulation of sub-optical cycle photocurrents in an ultrafast near-infrared scanning tunneling microscope, Opt. Express **33**, 48945 (2025).

[101] D. R. Ward, F. Hüser, F. Pauly, J. C. Cuevas, and D. Natelson, Optical rectification and field enhancement in a plasmonic nanogap, Nat. Nanotechnol. **5**, 732 (2010).

[102] M. Lenner, P. Rácz, P. Dombi, G. Farkas, and N. Kroó, Field enhancement and rectification of surface plasmons detected by scanning tunneling microscopy, Phys. Rev. B **83**, 205428 (2011).

[103] A. Dasgupta, M. Buret, N. Cazier, M. M. Mennemanteuil, R. Chacon, K. Hammani, J. C. Weeber, J. Arocas, L. Markey, G. C. des Francs, A. Uskov, I. Smetanin, and A. Bouhelier, Electromigrated electrical optical antennas for transducing electrons and photons at the nanoscale, Beilstein J. Nanotechnol. **9**, 1964 (2018).

[104] H. Ning, M. Maimaris, J. Wei, E. Gérouville, E. Moutoulas, Z. Meng, C. Ferchaud, D. Maslennikov, N. Mondal, T. Wang, C. Chow, A. P. Ivanov, J. B. Edel, S. A. Haque, M. Ivanov, J. P. Marangos, D. G. Georgiadou, and A. A. Bakulin, Ultrafast broadband strong-field tunneling in asymmetric nanogaps for time-resolved nanoscopy, arXiv:2405.12851.

[105] P. Zhang and Y. Y. Lau, Ultrafast strong-field photoelectron emission from biased metal surfaces: Exact solution to time-dependent Schrödinger equation, Sci. Rep. **6**, 19894 (2016).

[106] C. Voisin, N. Del Fatti, D. Christofilos, and F. Vallée, Ultrafast electron dynamics and optical nonlinearities in metal nanoparticles, J. Phys. Chem. B **105**, 2264 (2001).

[107] P. Grua, J. P. Morreeuw, H. Bercegol, G. Jonusauskas, and F. Vallée, Electron kinetics and emission for metal nanoparticles exposed to intense laser pulses, Phys. Rev. B **68**, 035424 (2003).

[108] L. V. Besteiro, X.-T. Kong, Z. Wang, G. Hartland, and A. O. Govorov, Understanding hot-electron generation and plasmon relaxation in metal nanocrystals: Quantum and classical mechanisms, ACS Photonics **4**, 2759 (2017).

[109] C. Ullrich, *Time-Dependent Density-Functional Theory: Concepts and Applications*, Oxford Graduate Texts (Oxford University Press, Oxford, 2019).

[110] H. O. Wijewardane and C. A. Ullrich, Time-dependent Kohn-Sham theory with memory, Phys. Rev. Lett. **95**, 086401 (2005).

[111] G. Vignale and W. Kohn, Current-dependent exchange-correlation potential for dynamical linear response theory, Phys. Rev. Lett. **77**, 2037 (1996).

[112] S. Zhou, X. Guo, K. Chen, M. T. Cole, X. Wang, Z. Li, J. Dai, C. Li, and Q. Dai, Optical-field-driven electron tunneling in metal-insulator-metal nanojunction, Adv. Sci. **8**, 2101572 (2021).

[113] Y. Luo, A. Martin-Jimenez, F. Neubrech, N. Liu, and M. Garg, Synthesis and direct sampling of single-cycle light transients by electron tunneling in a nanodevice, ACS Photonics **10**, 2866 (2023).

[114] W. Zhu, R. Esteban, A. G. Borisov, J. J. Baumberg, P. Nordlander, H. J. Lezec, J. Aizpurua, and K. B. Crozier, Quantum mechanical effects in plasmonic structures with sub-nanometre gaps, Nat. Commun. **7**, 11495 (2016).

[115] F. Monticone, N. A. Mortensen, A. I. Fernández-Domínguez, Y. Luo, X. Zheng, C. Tserkezis, J. B. Khurgin, T. V. Shahbazyan, A. J. Chaves, N. M. R. Peres, G. Wegner, K. Busch, H. Hu, F. D. Sala, P. Zhang, C. Ciracì, J. Aizpurua, A. Babaze, A. G. Borisov, X.-W. Chen, *et al.*, Nonlocality in photonic materials and metamaterials: Roadmap, Opt. Mater. Express **15**, 1544 (2025).

[116] G. Binnig, K. H. Frank, H. Fuchs, N. Garcia, B. Reihl, H. Rohrer, F. Salvan, and A. R. Williams, Tunneling spectroscopy and inverse photoemission: Image and field states, Phys. Rev. Lett. **55**, 991 (1985).

[117] J. I. Pascual, C. Corriol, G. Ceballos, I. Aldazabal, H.-P. Rust, K. Horn, J. M. Pitarke, P. M. Echenique, and A. Arnau, Role of the electric field in surface electron dynamics above the vacuum level, Phys. Rev. B **75**, 165326 (2007).

[118] H.-C. Ploigt, C. Brun, M. Pivetta, F. Patthey, and W.-D. Schneider, Local work function changes determined by field emission resonances: NaCl/Ag(100), Phys. Rev. B **76**, 195404 (2007).

[119] S. Liu, M. Wolf, and T. Kumagai, Plasmon-assisted resonant electron tunneling in a scanning tunneling microscope junction, Phys. Rev. Lett. **121**, 226802 (2018).